



Arrest of a radial hydraulic fracture upon shut-in of the injection

Andreas Möri, Brice Lecampion*

Geo-Energy Laboratory – Gaznat Chair on Geo-Energy, EPFL, Station 18, CH-1015 Lausanne, Switzerland

ARTICLE INFO

Article history:

Received 17 November 2020
Received in revised form 16 February 2021
Accepted 22 February 2021
Available online 6 March 2021

Keywords:

fracture arrest
shut-in
post-injection propagation
numerical methods

ABSTRACT

We investigate the propagation and arrest of a radial hydraulic fracture upon the end of the injection. Depending on the regime of propagation at the time of shut-in of the injection, excess elastic energy may be stored in the surrounding medium. Once the injection has stopped, the hydraulic fracture will arrest when the energy release rate falls under the material fracture energy. Fluid leaking-off to the surrounding medium acts as an energy sink such that the available excess energy for fracture growth decreases faster and as a result impacts the arrest (actually controls it in the zero toughness limit). Under the assumption of a homogeneous elastic medium and the Carter's leak-off model, we show that the post shut-in propagation of the hydraulic fracture depends on the dimensionless toughness \mathcal{K}_s and leak-off \mathcal{G}_s coefficient at the time of shut-in. Our investigation highlights that for an impermeable rock, the arrest radius is independent of the dimensionless toughness at shut-in. In the limit of a permeable rock with zero fracture toughness, the arrest radius is independent of the dimensionless leak-off coefficient only for $\mathcal{G}_s < 0.25$. For larger values of \mathcal{G}_s , the radius of arrest reduces with increasing \mathcal{G}_s . We delineate the limit above which the arrest is immediate upon shut-in. This limit is given by a critical leak-off coefficient at shut-in $\mathcal{G}_{s,c} \approx 0.53$ for the large leak-off/small toughness cases and by the relation $\mathcal{G}_{s,c}(\mathcal{K}_{s,c}) \approx 0.78 - 0.313 \cdot \mathcal{K}_{s,c}$ for small leak-off/large toughness (where $\mathcal{K}_{s,c}$ is equivalently the critical dimensionless toughness at shut-in). Immediate arrest in the impermeable limit is observed for $\mathcal{K}_{s,c} \approx 2.5$. If both (\mathcal{K}_s and \mathcal{G}_s) are smaller than their critical value for immediate arrest, post shut-in propagation occurs and a self-similar pulse viscosity storage solution emerges. Scaling arguments combined with numerical simulations, show that the propagation post shut-in scales as $1.23\mathcal{K}_s^{-2/5}$ in the impermeable and small leak-off cases, and as $0.75\mathcal{G}_s^{-2/13}$ in the zero toughness limit. The growth post shut-in can be significant in impermeable rocks - with a final radius up to twice larger than the radius at shut-in for realistic material and injection parameters.

© 2021 The Author(s). Published by Elsevier Ltd. This is an open access article under the CC BY-NC-ND license (<http://creativecommons.org/licenses/by-nc-nd/4.0/>).

1. Introduction

Hydraulic fractures (HF) are tensile fractures created by the injection of a fluid at pressure larger than the minimum in situ compressive stress (Detournay, 2016). The hydraulic fracturing technique is used in a broad range of engineering applications, from block caving mining (Jeffrey et al., 2013) to soil remediation (Germanovich and Murdoch, 2010), and is a cornerstone of hydrocarbon production from low permeability shales (Smith and Montgomery, 2015). Such tensile fluid-driven fractures also propagate naturally in the form of magmatic intrusion in the upper earth crust, forming volcanic dikes and sills (Rivalta et al., 2015; Spence et al., 1987; Lister and Kerr, 1991). The growth of HF's is governed by a strong coupling between linear elastic fracture mechanics (LEFM), lubrication flow in the propagating fracture, and leak-off

of the fluid into the surrounding medium. The competition between these different physical processes is now well understood for a growing fracture under a constant injection rate and results in various growth regimes (Detournay, 2004, 2016). The propagation of an HF is dependent on the relative importance of two storage and two dissipative mechanisms. The bulk of the injected fluid either remains in the propagating fracture or leaked-off in the surrounding medium (storage vs. leak-off dominated regimes) while the energy is either dissipated in the creation of new fracture surfaces or the viscous flow within the fracture (toughness vs. viscosity dominated regimes). For simple geometries (plane-strain and radial), solutions for hydraulic fracture growth have been obtained in these limiting regimes, leveraging the multiscale asymptotic solution of a steadily moving semi-infinite hydraulic fracture (Garagash et al., 2011). These theoretical predictions compare well with experiments performed in impermeable materials, notably for radial fractures (Bunger and Detournay, 2008; Lecampion et al., 2017). The evolution of a radial hydraulic fracture after the

* Corresponding author.

E-mail address: brice.lecampion@epfl.ch (B. Lecampion).

end of the injection (often referred to as shut-in in industrial applications) is the topic of this paper. In particular, we aim at quantitatively answering two important questions: under what conditions does the fracture immediately arrest? and if it does not arrest immediately, how far does it propagate before finally arresting?

Interestingly, these questions have been seldomly looked at in detail despite the importance of fracture closure in industrial applications. A large body of work has indeed investigated the closure problem but generally treated the arrest in an ad hoc manner and/or did not quantitatively investigate the parameters controlling post-shut-in propagation and arrest. Modeling fracture closure aims to better interpret the pressure decline curve measured after shut-in. These measurements are used to estimate relevant parameters (in situ stress, pore-pressure among others) for the design of well stimulation treatments by hydraulic fracturing (Economides and Nolte, 2000). One of the first models of fracture closure (Nolte, 1979) assumed a constant area upon the end of the injection (and as such an immediate arrest) for a fracture of constant height (Perkins-Kern-Nordgren (PKN) geometry). Settari and Cleary (1984) implemented a pseudo-3D model to address the problem in a more general way and additionally allowed for post-injection propagation. They observed a slight post-shut-in propagation in some of their investigated cases without going into details. Gu and Leung (1993) extended the analysis to three-dimensional planar fractures accounting for non-uniform in situ stresses and leak-off parameters but did not account for any post-injection growth. Desroches and Thiercelin (1993) model fracture growth and closure for simple geometries (plane-strain and axisymmetric fractures) in a fully coupled manner based on the now classical hypothesis of LEFM, lubrication flow, and Carter's leak-off. They observe a small amount of propagation after shut-in in some of the cases investigated: the complete analysis of this post-shut-in propagation is, however, not treated. Papanastasiou (2000) investigated numerically propagation and closure (accounting also for bulk plasticity). The effect of poroelasticity on fracture closure is mentioned in the work of Boone and Ingraffea (1990) and Detournay et al. (1989) on the modeling of small hydraulic fracturing tests. Recently, the 2D plane-strain problem has been revisited numerically using an extended finite element method (Mohammadnejad and Andrade, 2016). These different modeling works, as well as experimental observations (De Pater et al., 1996; van Dam et al., 2000; Zanganeh et al., 2017), agree on the conclusion that propagation after shut-in can occur in some cases. The problem of fracture arrest was quantified in detail only in the large toughness limit for a plane strain hydraulic fracture propagating in an impermeable medium by Garagash (2006a). In that large toughness limit (limit of small dimensionless viscosity \mathcal{M}), the additional propagation post-shut-in (with respect to the length at shut-in) scales as $2.9\mathcal{M}$ for $\mathcal{M} \ll 1$ (Garagash, 2006a).

We focus here in detail on the case of a radial fracture and quantify the final HF's arrest radius as a function of rock, fluid properties, and injection duration, accounting for both fluid leak-off and fracture toughness. We combine scaling analysis and numerical simulations to do so. One can easily anticipate a series of different behavior as a function of the amount of elastic energy stored in the medium still available upon shut-in (see Appendix A for the complete energy budget). When viscous flow dissipation dominates at shut-in, and thus some excess elastic energy is still available, the fracture will keep growing for a while. On the other hand, it will likely immediately arrest if fracture energy dominates the overall energy dissipation at shut-in. Similarly, a larger leak-off intensity acts as an energy sink reducing the energy available for growth and thus will lead to an earlier arrest after the end of the injection.

We first present the mathematical formulation of the problem, its scaling, and outline the numerical solver used. We then

treat first the impermeable case before moving to the case of a permeable medium with zero and finally finite fracture toughness.

2. Problem formulation

We focus on a radial hydraulic fracture propagating in a linear isotropic homogeneous elastic medium driven by a Newtonian fluid. Similarly to previous contributions (Savitski and Detournay, 2002; Madyarova, 2003), we neglect the size of the injected well-bore compared to the fracture size and model the injection as a point source. The fluid leak-off in the surrounding medium is modeled using Carter's leak-off model which amounts to an early time 1D approximation of fluid diffusion valid when the net pressure is small compared to the far-field in situ effective stress (see for example Lecampion et al., 2018; Kanin et al., 2020 for further discussion). We also neglect the presence of a fluid lag – an assumption which is valid as soon as the shut-in time is larger than the characteristic time-scale $t_{om} = \frac{\mu' E'^2}{\sigma_o^2}$ controlling the coalescence of the fluid and fracture fronts (Garagash, 2006b; Lecampion and Detournay, 2007; Bungler and Detournay, 2007). We briefly recall the governing equations of the coupled moving boundary hydro-mechanical fracture problem. In line with previous contributions, we use the following material constants for clarity

$$E' = \frac{E}{1 - \nu^2}, \quad K' = 4\sqrt{\frac{2}{\pi}}K_{Ic}, \quad \mu' = 12\mu, \quad C' = 2C_L \quad (1)$$

where C_L is the Carter leak-off coefficient, K_{Ic} the fracture toughness, μ the fluid viscosity, E and ν the material elastic Young's modulus and Poisson's ratio respectively.

Quasi-static elasticity relates the fracture width w to the net pressure loading at the fracture faces $p = p_f - \sigma_o$ (the fluid pressure in excess of the in situ compressive stress). For such a purely tensile axisymmetric fracture, the elastic problem reduces to the following integral representation (Sneddon, 1951)

$$w(\rho, t) = \frac{8}{\pi} \frac{R(t)}{E'} \int_{\rho}^1 \frac{\xi}{\sqrt{\xi^2 - \rho^2}} \int_0^1 \frac{x p(x\xi R, t)}{\sqrt{1 - x^2}} dx d\xi \quad (2)$$

or alternatively its inverse (Gordeliy and Detournay, 2011). Under the assumption of quasi-static linear elastic fracture mechanics, the fracture propagation conditions for fracturing under pure mode I read:

$$(K_I - K_{Ic}) \frac{dR(t)}{dt} = 0 \quad \frac{dR(t)}{dt} \geq 0 \quad (3)$$

where the stress intensity factor K_I can be estimated via the Bueckner-Rice integral (Rice, 1972)

$$K_I = \frac{2}{\sqrt{\pi R(t)}} \int_0^{R(t)} \frac{p(t, r)}{\sqrt{R^2 - r^2}} r dr \quad (4)$$

Fluid flow in the fracture is modeled under the lubrication approximation (Batchelor, 1967). The fluid continuity equation combined with Poiseuille's law for a Newtonian fluid yields the following Reynolds equation

$$\frac{\partial w(t, r)}{\partial t} - \frac{1}{\mu'} \frac{1}{r} \frac{\partial}{\partial r} \left(r w(t, r)^3 \frac{\partial p(t, r)}{\partial r} \right) + \frac{C'}{\sqrt{t - t_o(r)}} = 0 \quad (5)$$

which states that the change of fracture aperture (first term) is balanced by the in/out fluid fluxes (second term) and the rate of fluid leaking out of the fracture into the rock following Carter's law (third term). Integration in space and time gives the global fluid volume balance which relates the injected volume $V(t)$ to the fracture and fluid leak-off volumes:

$$V(t) = 2\pi \int_0^R w(t, r) r dr + 2\pi \int_0^t \int_0^R \frac{2C_L}{\sqrt{\tau - \tau_o(r)}} r dr d\tau \quad (6)$$

where the boundary condition of zero fracture width and zero fluid flux at the fracture tip have been used. We assume a simple history for the injection: a constant injection at a rate Q_o up to a time t_s when the pump is “shut-in” such that

$$V(t) = Q_o t, \text{ for } t < t_s; V(t) = Q_o t_s = V_o, \text{ for } t \geq t_s \quad (7)$$

2.1. Growth during constant injection ($t < t_s$)

Hydraulic fracture growth during the injection period ($t < t_s$) is well understood for such a radial geometry (Savitski and Detournay, 2002; Detournay, 2004, 2016) and can be summarized in a rectangular propagation diagram (see Fig. 1b following Detournay (2016)). Notably, the HF growth evolves from a regime initially dominated by viscous dissipation and fluid storage inside the fracture (M -vertex in Fig. 1b) to a regime dominated by fracture toughness and fluid leak-off at large-time (\tilde{K} -vertex in Fig. 1b). The complete evolution of the fracture is governed by a time-dependent dimensionless fracture toughness \mathcal{K}_m (or alternatively dimensionless viscosity \mathcal{M}_k) and a time-dependent dimensionless leak-off coefficient \mathcal{C} (or alternatively dimensionless storage \mathcal{S}). The dimensionless parameters \mathcal{K}_m and \mathcal{C}_m can be expressed as a function of two time-scales t_{mk} and $t_{m\tilde{m}}$ governing the transition from the viscous/storage dominated regime to respectively the toughness/storage and viscous/leak-off regimes:

$$\mathcal{K}_m = (t/t_{mk})^{1/9} \quad \mathcal{C}_m = (t/t_{m\tilde{m}})^{7/18} \quad t_{mk} = \frac{E^{13/2} \mu^{5/2} Q_o^{3/2}}{K^9} \quad t_{m\tilde{m}} = \frac{\mu^{4/7} Q_o^{6/7}}{C^{18/7} E^{4/7}} \quad (8)$$

The complete evolution of the solution from the viscosity/storage dominated to the toughness/leak-off regime within the propagation diagram of Fig. 1b can be grasped by a trajectory parameter

$$\phi = \left(\frac{t_{mk}}{t_{m\tilde{m}}} \right)^{14/9} = \frac{C^4 E^{11} \mu^3 Q_o}{K^{14}} = \mathcal{C}_m^4 / \mathcal{K}_m^{14} \quad (9)$$

and the dimensionless time t/t_{mk} . The growth solution can be adequately expressed using specific scalings for different propagation regimes, writing the fracture radius, width, and net pressure as

$$R(t) = L(t) \gamma(\mathcal{P}_1, \mathcal{P}_2) \quad w(r, t) = W(t) \Omega(r/R, \mathcal{P}_1, \mathcal{P}_2) \\ p(r, t) = P(t) \Pi(r/R, \mathcal{P}_1, \mathcal{P}_2)$$

where $P(t) = E'W(t)/L(t)$ is the characteristic pressure scale, $L(t)$ and $W(t)$ the characteristic fracture length and width scales while $\mathcal{P}_1, \mathcal{P}_2$ denote the corresponding two dimensionless parameters (e.g. dimensionless toughness and leak-off in the viscosity scaling). We refer to Detournay (2016) for the details of the constant injection case ($t_s \rightarrow \infty$).

2.2. Evolution post-shut-in ($t > t_s$)

For the case of a finite injection/pulse injection, after the shut-in time ($t > t_s$), the growth of the hydraulic fracture can be grasped using similar scaling arguments by substituting the finite injected volume $V_o = Q_o t_s$ in place of the rate-dependent volume $Q_o t$. In other words, by replacing Q_o with V_o/t in the constant injection scalings. The scales and evolution parameters for the four different regimes (viscosity/toughness, leak-off/storage) in this case are presented in Table 1. Whenever we refer to the constant injection scaling, the superscript will be omitted (for example, L_m denotes the characteristic length scale of the viscosity storage constant injection scaling). On the other hand, the constant volume/pulse injection scaling is indicated by the superscript $[V]$ (for example, $L_m^{[V]}$ denotes the characteristic length scale of the viscosity storage pulse injection scaling).

It is interesting to note that the lengthscales $L^{[V]}$ in both leak-off dominated scalings ($\tilde{M}^{[V]}$ and $\tilde{K}^{[V]}$) listed in Table 1 are decaying with time. This indicates that for a finite volume injection if dominated by leak-off, the fracture recesses. This hints toward an immediate arrest after shut-in in those cases. Similarly, we observe that the fracture lengthscale is time-independent in the toughness/storage scaling ($K^{[V]}$ in Table 1). The fracture lengthscale increases with time only in the viscosity/storage dominated regime ($M^{[V]}$ in Table 1). We already get a grasp at the structure of the solution after shut-in from those observations and anticipate that if the shut-in occurs when the fracture is already propagating in the leak-off dominated regime, it will immediately arrest and actually recess. If leak-off is negligible at shut-in, the fracture will continue to grow if dominated by viscosity while it will tend to a constant size if dominated by fracture toughness, and as such arrest in a finite time.

Our aim in what follows is to investigate the post-shut-in stages thoroughly and delineate when and how further growth after shut-in occurs. To do so, we will combine scaling arguments and semi-analytical solutions in some limiting regimes with full numerical solutions. This evolution post-shut-in will be dependent on the

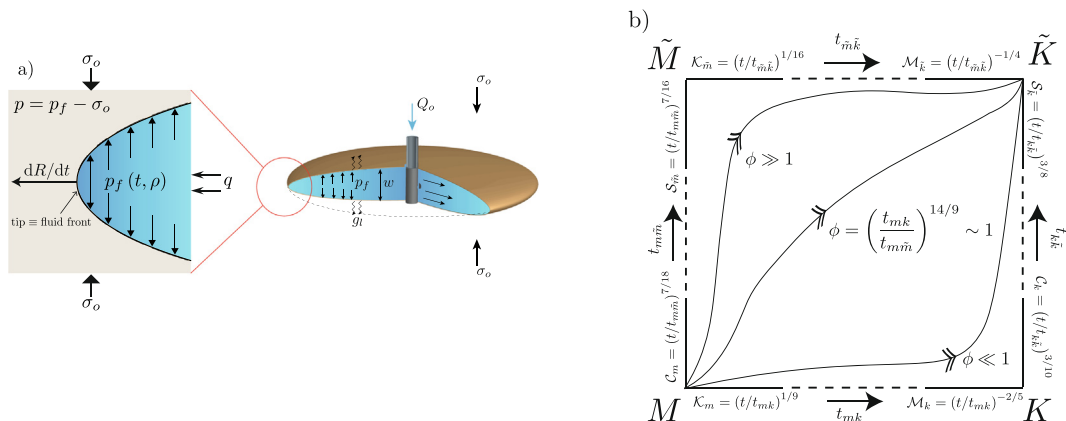


Fig. 1. a) Sketch of a radial hydraulic fracture with a zoom on the HF tip viewed as a steadily moving plane-strain case. b) Evolution of the fracture propagation regime for a radial fracture in a linear elastic permeable medium with Carter's leak-off - following Detournay (2016).

Table 1

Characteristic scales and evolution parameters in the four propagation regimes for post-shut-in evolution (pulse injection case).

| Scaling | $M^{[V]}$ | $K^{[V]}$ | $\tilde{M}^{[V]}$ | $\tilde{K}^{[V]}$ |
|---------------------|--|--|---|--|
| $L^{[V]}$ | $\frac{E^{1/9} t^{1/9} V_o^{1/3}}{\mu^{1/9}}$ | $\frac{E^{2/5} V_o^{2/5}}{K^{2/5}}$ | $\frac{V_o^{1/2}}{C^{1/2} t^{1/4}}$ | $\frac{V_o^{1/2}}{C^{1/2} t^{1/4}}$ |
| $p^{[V]}$ | $\frac{E^{2/3} \mu^{1/3}}{t^{1/3}}$ | $\frac{K^{6/5}}{E^{1/5} V_o^{1/5}}$ | $\frac{\mu^{1/4} C^{3/8} E^{3/4}}{V_o^{1/8} t^{1/16}}$ | $\frac{K' C^{1/4} t^{1/8}}{V_o^{1/4}}$ |
| $W^{[V]}$ | $\frac{V_o^{1/3} \mu^{2/9}}{E^{2/9} t^{2/9}}$ | $\frac{V_o^{1/5} K^{4/5}}{E^{4/5}}$ | $\frac{\mu^{1/4} V_o^{3/8}}{E^{1/4} C^{1/8} t^{5/16}}$ | $\frac{K' V_o^{1/4}}{E' C^{1/4} t^{1/8}}$ |
| $\mathcal{K}^{[V]}$ | $\frac{K'}{E^{13/18} \mu^{5/18} V_o^{3/18}}$ | 1 | $\frac{K' t^{3/16}}{\mu^{1/4} C^{1/8} E^{3/4} V_o^{1/8}}$ | 1 |
| $\mathcal{M}^{[V]}$ | 1 | $\frac{\mu' E^{13/5} V_o^{3/5}}{K^{18/5} t}$ | 1 | $\mu' \frac{V_o^{1/2} E^3 C^{1/2}}{K^4 t^{3/4}}$ |
| $\mathcal{C}^{[V]}$ | $\frac{C' E^{2/9} t^{13/18}}{V_o^{1/3} \mu^{2/9}}$ | $\frac{C' E^{4/5} t^{1/2}}{V_o^{1/3} K^{4/5}}$ | 1 | 1 |
| $\mathcal{S}^{[V]}$ | 1 | 1 | $\frac{E^{1/4} C^{9/8} t^{13/16}}{\mu^{1/4} V_o^{3/8}}$ | $\frac{E' C^{5/4} t^{5/8}}{K' V_o^{1/4}}$ |

dimensionless toughness and dimensionless leak-off coefficients at shut-in

$$\begin{aligned}\mathcal{K}_s &= \mathcal{K}_m(t = t_s) = \mathcal{K}_m^{[V]}(t = t_s) = K' \frac{t_s^{1/9}}{E^{13/18} \mu^{5/18} Q_o^{1/6}} \\ \mathcal{C}_s &= \mathcal{C}_m(t = t_s) = \mathcal{C}_m^{[V]}(t = t_s) = C' \frac{E^{2/9} t_s^{7/18}}{Q_o^{1/3} \mu^{2/9}}.\end{aligned}\quad (10)$$

where $V_o = Q_o t_s$ has been used. Alternatively, the evolution can be grasped as a function of one of the two shut-in parameters (\mathcal{K}_s or \mathcal{C}_s) and the trajectory parameter $\phi = (t_{mk}/t_{m\bar{m}})^{14/9} = \mathcal{C}_m^4/\mathcal{K}_m^{14} = \mathcal{C}_s^4/\mathcal{K}_s^{14}$.

2.3. Numerical solver used

We will use extensively the open source-planar 3D hydraulic fracture simulator PyFrac (Zia and Lecampion, 2020). The code is a python implementation of the implicit level set algorithm (ILSA) (Peirce and Detournay, 2008) for three-dimensional planar HF. The scheme notably combines a finite discretization of the fracture with the use of the near tip HF asymptotic solution (see for example Garagash et al. (2011)), valid close to the moving boundary of the HF (at the tip, see Fig. 1a). We briefly outline the numerical techniques used to solve the governing equations presented in Section 2 and refer to Zia and Lecampion (2020) for more details.

The fracture propagation plane is discretized using a rectangular Cartesian mesh with constant cell size. The fracture front is defined via a level-set evaluated at the center of each cell. The algorithm marches in time such that the solution at time t^{n+1} is obtained from the known solution at t^n . The solution at a given time consists of the level set field (closest distance to the front from a cell center), the fracture front (location of intersections with cell edges), fracture opening, and fluid pressure inside the fracture (defined at the center of the cells). Quasi-static elasticity is discretized using a displacement discontinuity method with piecewise constant rectangular elements, while the Reynolds Eq. (5) is discretized spatially via a finite volume method. The fluid fluxes are notably obtained at the cell edges via a central finite difference scheme. After accounting for the injected volume during $\Delta t^{n+1} = t^{n+1} - t^n$, using a fully implicit time-integration scheme, one obtains a non-linear (elastohydrodynamic) system of equations for a given trial fracture front position. This non-linear sys-

tem is solved via Anderson acceleration of fixed-point iterations (Anderson, 1965; Walker and Ni, 2011). Once the elastohydrodynamic system is solved, a new fracture front position is found using the ILSA scheme. This scheme updates the values of the level set function according to the widths in the ribbon elements close to the tip, obtained from the elastohydrodynamic system. An iteration procedure between the front-location and the resolution of the elastohydrodynamic system (for a given fracture front position) is performed until the fracture front converges between subsequent iterations. We use the approximation of the universal tip asymptote provided by Dontsov and Peirce (2017). For computational efficiency and robustness, we use a predictor–corrector scheme for the fracture front advancing scheme where the starting point of the iteration on the fracture front is obtained with an explicit time step using the velocity obtained in the previous time step (see Zia and Lecampion, 2019 for more details). The scheme has been extensively tested against known solutions and proved to be robust and accurate (Peirce, 2015, 2016; Zia et al., 2018; Zia and Lecampion, 2020; Moukhtari et al., 2020). In what follows, all the reported simulations use a grid size of 61×61 elements, and a re-meshing (coarsening of the element size by a factor 2) is performed when the fracture reaches the end of the grid, such that at most the fracture contains approximately 61×61 elements and at minimum 30×30 elements (for details on numerical accuracy see Appendix B).

3. Impermeable medium

For the case of an impermeable medium, the fracture will arrest when the excess elastic energy present at shut-in falls below the energy required for subsequent fracture growth.

3.1. Arrest radius in the finite toughness case

If the fracture toughness is finite, the arrest will occur when the stored elastic energy present at shut-in has been entirely consumed by viscous flow. When the fluid velocity vanishes, the fluid pressure is uniform inside the fracture (as per Poiseuille law's $v = -w^2/\mu' \partial p/\partial z = 0 \rightarrow \partial p/\partial z = 0$). The radius of arrest is simply obtained as the solution of the quasi-static equilibrium of a crack under uniform net loading p with a prescribed volume V_o for which the stress intensity factor is strictly equal to K_{Ic} . For a uniform net pressure p , the elasticity (2) reduces to (Sneddon, 1946)

$$w(r) = \frac{8}{\pi} \frac{p}{E'} \sqrt{R^2 - r^2} \quad (11)$$

and the fracture volume V_f and mode I stress intensity factor are given as

$$V_f = \frac{16}{3} \frac{pR^3}{E'} \quad (12)$$

$$K_I = \frac{2}{\sqrt{\pi}} pR^{1/2} \quad (13)$$

In the absence of leak-off (impermeable case), imposing that the fracture volume equals the injected volume V_o and that the stress intensity factor K_I equals the fracture toughness, one can easily solve for the corresponding radius, net pressure, and width:

$$R_{k,a} = \left(\frac{3}{\pi\sqrt{2}} \right)^{2/5} \left(\frac{E'V_o}{K'} \right)^{2/5}, \quad (14a)$$

$$p_{k,a} = \left(\frac{\pi^6}{3 \times 2^{17}} \right)^{1/5} \left(\frac{K'^6}{E'V_o} \right)^{1/5}, \quad (14b)$$

$$w_{k,a}(r) = \left(\frac{3}{8\pi} \right)^{1/5} \sqrt{1 - \left(\frac{r}{R_{k,a}} \right)^2} \left(\frac{V_o K'^4}{E'^4} \right)^{1/5}. \quad (14c)$$

We shall denote this solution as the toughness arrest solution (with subscript k, a). It only depends on the rock properties (elasticity and toughness) and the total volume injected. This solution (Eqs. (14a)–(14c)) corresponds to the $K^{[V]}$ -Vertex characteristic scales multiplied by prefactors of order one. It is also worth noting that the solution for a toughness dominated growth under constant injection rate (see Abé et al. (1976, 2002)) is merely obtained by replacing V_o by $Q_o t$ in this solution.

3.2. Viscosity-storage pulse solution in the zero toughness limit - case of no arrest

In the limit of zero toughness (for example when re-opening a pre-existing fracture), we see from (14a) that the arrest radius becomes infinite. In other words, in that limit, the hydraulic fracture will continue to grow ad vitam æternam. Given the scaling of Table (1) in this regime of zero toughness and zero leak-off, the growth of an HF with a finite volume V_o does not depend on any dimensionless parameter ($\mathcal{K}_m^{[V]} = \mathcal{G}_m^{[V]} = 0$). As a result, the growth is self-similar, and a solution can be derived using the viscosity/storage $M^{[V]}$ scaling. Eqs. (2)–(6) in the $M^{[V]}$ scaling can be rewritten as:

$$\bar{\Omega}_{m0}^{[V]}(\rho) = \frac{8}{\pi} \int_{\rho}^1 \frac{\xi}{\xi^2 - \rho^2} \int_0^1 \frac{x \Pi_{m0}^{[V]}(\rho)}{\sqrt{1 - x^2}} dx d\xi \quad (15a)$$

$$\frac{1}{9} \rho + \left(\bar{\Omega}_{m0}^{[V]}(\rho) \right)^2 \frac{d\Pi_{m0}^{[V]}(\rho)}{d\rho} = 0 \quad (15b)$$

$$\int_0^1 \frac{\Pi_{m0}^{[V]}(\rho)}{\sqrt{1 - \rho^2}} \rho d\rho = 0 \quad (15c)$$

$$\gamma_{m0}^{[V]} = \left(2\pi \int_0^1 \bar{\Omega}_{m0}^{[V]}(\rho) \rho d\rho \right)^{-1/3} \quad (15d)$$

subjected to the boundary conditions of zero dimensionless opening and fluid flux at the tip. The dimensionless solution $\mathcal{F}_{m0}^{[V]}$ (where the subscript $m0$ refer to the zero toughness/leak-off limit) consists

of the dimensionless fracture radius $\gamma_{m0}^{[V]}$, net pressure $\Pi_{m0}^{[V]}$, and reduced opening $\bar{\Omega}_{m0}^{[V]}(\rho) = \Omega_{m0}^{[V]}(\rho)/\gamma_{m0}^{[V]}$.

This set of equations can be solved numerically using Gauss–Chebyshev quadrature and barycentric Lagrange differentiation and interpolation. Such a numerical method follows previous work (Viesca and Garagash, 2018; Liu et al., 2019) and is described in Appendix B. The dimensionless opening and pressure profiles are shown in Fig. 10 of Appendix B. The dimensionless fracture length obtained numerically is $\gamma_{m0}^{[V]} \approx 0.8360$. We also note that the numerical results obtained using PyFrac matches very well the one obtained via this Gauss–Chebyshev based scheme (see Table 6 in Appendix B).

3.3. Propagation and arrest post-shut-in

We now turn to investigate the propagation after shut-in in the impermeable case and the subsequent arrest due to a finite toughness numerically.

In the case of growth after shut-in (pulse injection) for a finite toughness in an impermeable medium, the final radius of arrest is given by Eq. (14a), and the growth solution toward this arrest only depends on a dimensionless toughness $\mathcal{K}_m^{[V]}(t)$ (see Table 1) which can be expressed as a function of the dimensionless toughness at shut-in $\mathcal{K}_s = \mathcal{K}_m(t_s)$:

$$\mathcal{K}_m^{[V]}(t) = \left(\frac{t}{t_s} \right)^{5/18} \mathcal{K}_s. \quad (16)$$

The evolution of the fracture radius as a function of t/t_s for a series of simulations with different values of \mathcal{K}_s (equivalent to different shut-in time) is displayed in Fig. 2. The radius is scaled by the final arrest radius $R_{k,a}$ (14a). We note that during the injection phase ($t/t_s < 1$), we retrieve the semi-analytical solutions of growth under a constant injection rate derived in Savitski and Detournay (2002) (red (toughness dominated) and blue (viscosity dominated) dashed lines in Fig. 2). Upon shut-in, the behavior of the fracture changes depending on the dimensionless toughness at shut-in \mathcal{K}_s . However, the arrest radius is uniquely defined (it does not depend on \mathcal{K}_s) and equals, up to numerical precision (between 1 to 3.5% relative error), to the theoretical value given by Eq. (14a). For small values of \mathcal{K}_s (where the shut-in happens when the HF is in the viscosity dominated regime), one observes the transition from the constant injection rate viscosity solution (Savitski

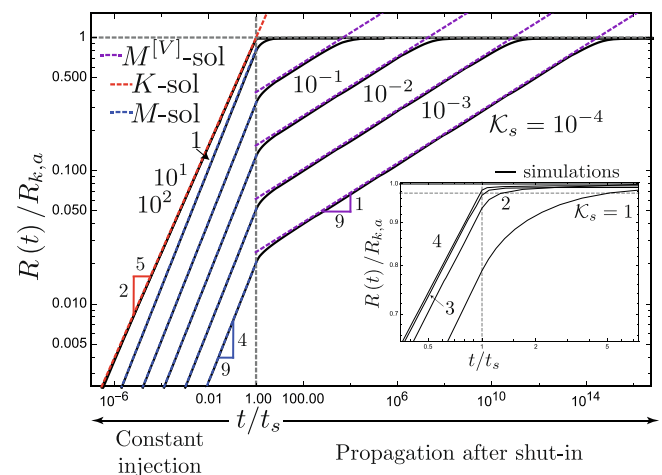


Fig. 2. Normalized fracture radius as function of the dimensionless shut-in time t/t_s . Numerical (and semi-analytical) predictions of fracture radius scaled by the arrest radius $R_{k,a}$ (14a) for various values of shut-in toughness \mathcal{K}_s (10) (from 10^{-4} to 10^2).

and Detournay, 2002) to the pulse viscosity dominated solution discussed in Section 3.2 (dashed magenta line on Fig. (2)). This self-similar propagation appears at intermediate times before the fracture finally arrests at a radius equal to $R_{k,a}$ (14a). Larger values of $\mathcal{K}_s \gtrsim 3$ result in an immediate arrest as the stored elastic energy is already balanced by fracture energy at shut-in: the radius at shut-in is equal to the arrest radius.

We post-process these results in order to estimate the limiting value of $\mathcal{K}_{s,c}$ (c for critical) above which immediate arrest occurs after shut-in. We define immediate arrest at shut-in when the radius at shut-in $R_s = R(t = t_s)$ is equal or larger to 97.5% of the final arrest radius ($R_s/R_{k,a} \geq 0.975$). In other words, when the radius at shut-in is within 2.5% of the toughness/arrest dominated solution (14a). We obtain $\mathcal{K}_{s,c} \approx 2.75 \pm 0.2$ from our series of numerical simulations. Such an estimate is in line with the one that can be derived from the first-order propagation solution for large toughness (dimensionless radius $\gamma_m \approx 0.8546\mathcal{K}^{-2/5} - 0.7349\mathcal{K}^{-4}$ expressed in the viscosity scaling – see Savitski and Detournay (2002)). Savitski and Detournay (2002) estimate $\mathcal{K} \approx 3.5$ for a fully toughness dominated growth assuming a 1% relative difference between the zero $0.8546\mathcal{K}^{-2/5}$ and first-order $(0.8546\mathcal{K}^{-2/5} - 0.7349\mathcal{K}^{-4})$ solutions. One obtains $\mathcal{K} \approx 2.67$, respectively $\mathcal{K} \approx 2.5$ when taking 2.5% respectively 3% relative difference. These values are consistent with the estimate directly derived from our numerical simulations. We take $\mathcal{K}_{s,c} \approx 2.5$ for simplicity in the following – in line with the upper bound of the relative error of our numerical solution (between 1 to 3.5% relative accuracy with respect to self-similar growth solutions for the mesh resolution used here, see Appendix B).

For the case of dimensionless shut-in toughness lower than $\mathcal{K}_{s,c}$, the fracture continues to grow after shut-in up to the arrest radius $R_{k,a}$. When the fracture propagates in the viscosity dominated regime at shut-in ($\mathcal{K}_s \ll 1$ cases), the distance propagated after shut-in can be estimated by simply comparing the final arrest radius $R_{k,a}$ (see Eq. (14a)) with the radius of the fracture at shut-in ($t = t_s$) from the constant injection viscosity dominated solution (Savitski and Detournay, 2002):

$$R_m(t = t_s) = R_s = 0.6978 \frac{E^{1/9} Q_0^{1/3} t_s^{4/9}}{\mu^{1/9}} \quad (17)$$

We thus obtain the following relation between the arrest and shut-in radius and the dimensionless toughness at shut-in:

$$\frac{R_{k,a}}{R_s} = \frac{\left(\frac{3}{\pi\sqrt{2}}\right)^{2/5} \left(\frac{E'V_a}{K'}\right)^{2/5}}{0.6978 \left(\frac{E^{1/9} Q_0^{1/3} t_s^{4/9}}{\mu^{1/9}}\right)} \approx 1.23 \mathcal{K}_s^{-2/5} \quad (18)$$

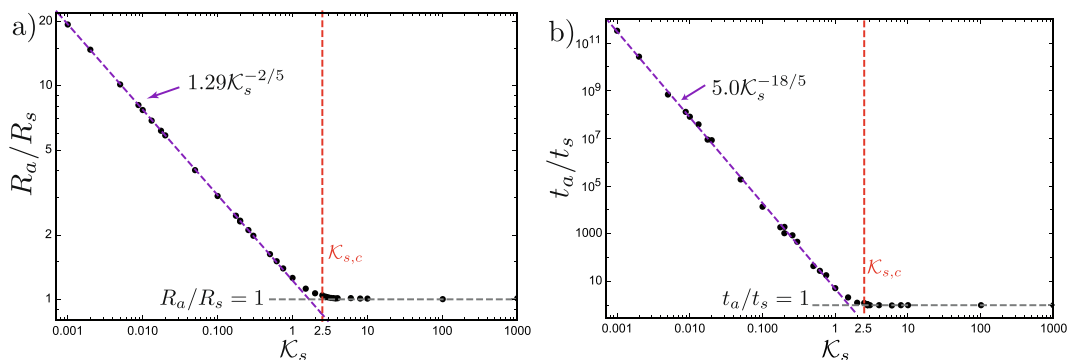


Fig. 3. Characteristical values of post-injection propagation in function of the dimensionless toughness at shut-in \mathcal{K}_s (impermeable case). a) Ratio between arrest and shut-in radius for a radial fracture in an impermeable medium. b) Time of arrest over shut-in time. Numerical simulations (Black dots) and analytical estimate for small \mathcal{K}_s (dashed purple line).

Fig. 3 shows that this semi-analytical approximation falls exactly on our numerical results for values of \mathcal{K}_s below 1. It slightly underestimates the ratio R_a/R_s for values of the dimensionless shut-in toughness between 1 and the value for immediate arrest $\mathcal{K}_{s,c} \approx 2.5$. This is simply because, for values of \mathcal{K}_s larger than one, the estimate of the radius at shut-in provided by the constant injection viscosity dominated (zero toughness) solution is no longer a valid approximation as the fracture toughness impacts the solution.

From Eq. (16), we can similarly estimate the following relation between the shut-in time ($t = t_s$) and the time of arrest ($t = t_a$):

$$\frac{t_a}{t_s} \propto \mathcal{K}_s^{-18/5}. \quad (19)$$

We use our numerical simulations to capture the corresponding prefactor leading to the relation $t_a/t_s \approx 5.0\mathcal{K}_s^{-18/5}$, again valid for \mathcal{K}_s smaller than 1. Fig. 3 illustrates that the time of arrest can be significantly larger than the shut-in time for values of \mathcal{K}_s smaller than the critical value for immediate arrest $\mathcal{K}_{s,c} \approx 2.5$.

4. Permeable medium

We now switch to the case of a permeable medium. The loss of fluid in the surrounding rock is an additional arresting mechanism after shut-in as it acts as an energy sink for the excess of elastic energy available for subsequent growth. We, therefore, anticipate that the arrest radius may significantly differ from the impermeable estimate given by Eq. (14a).

4.1. Zero toughness case

In the zero toughness case, the arrest is solely governed by the loss of fluid and no analytical or semi-analytical expressions are currently available for the post-shut-in phase. As mentioned previously, the scaling for a pulse HF indicates an immediate recession in the viscosity/leak-off regime ($\tilde{M}^{(V)}$). We can thus anticipate an immediate arrest if the shut-in occurs when the HF already propagates in the so-called viscosity/leak-off dominated regime (\tilde{M}). In the constant injection case (prior to shut-in), the transition from the viscosity/storage (M) to the viscosity/leak-off (\tilde{M}) regime is governed by a dimensionless leak-off coefficient $\mathcal{C}_m(t) = (t/t_{mm})^{7/18}$ (see Eq. (8)). The leak-off/viscosity dominated solution is fully reached within 1% for $\mathcal{C}_m \approx 13$, and within 3% for $\mathcal{C}_m \approx 4$ (Madyarova, 2003; Dontsov, 2016).

In the zero toughness case, the growth after shut-in is governed solely by the dimensionless leak-off coefficient

$$\mathcal{C}_m^{[V]}(t) = \left(\frac{t}{t_s}\right)^{13/18} \mathcal{C}_s.$$

Similarly to the impermeable case, the dimensionless leak-off coefficient at shut-in \mathcal{C}_s (10) will govern the arrest of the fracture. We can hypothesize that fracture arrest will occur when the HF enters the viscosity/leak-off regime ($\tilde{M}^{[V]}$). This is equivalent to stating that $\mathcal{C}_m^{[V]} \sim 1$ such that we can estimate the time of arrest as

$$t_{\tilde{m},a} \sim t_s \mathcal{C}_s^{-18/13}. \quad (20)$$

The estimation of the arrest radius then emerges from the scaling (Table 1) as

$$R_{\tilde{m},a} = \gamma_{\tilde{m},a} L_m^{[V]}(t = t_{\tilde{m},a}) = \gamma_{\tilde{m},a} \times \frac{E^{1/13} V_o^{5/13}}{C^{2/13} \mu^{1/13}} \quad (21)$$

where $\gamma_{\tilde{m},a}$ is an unknown constant of order 1.

We perform a series of simulations for different values of \mathcal{C}_s ranging from 10^{-15} to 10^2 . The arrest radius as a function of \mathcal{C}_s is displayed in Fig. 4. We confirm that indeed the arrest radius scales with $L_m^{[V]}(t = t_{\tilde{m},a})$. In addition, two regimes can be observed. For $\mathcal{C}_s \lesssim 0.25$, the arrest radius scaled by $L_m^{[V]}(t = t_{\tilde{m},a})$ is indeed strictly constant, while for large values of \mathcal{C}_s the arrest is immediate such that the arrest radius corresponds to the radius at shut-in given by the large leak-off propagation solution (\tilde{M} -solution).

More precisely, for $\mathcal{C}_s \lesssim 0.25$, we can estimate the pre-factor of the exact arrest radius which scales with $L_m^{[V]}(t = t_{\tilde{m},a})$. We obtain $\gamma_{\tilde{m},a} \approx 0.5218$ from a linear regression of our numerical results, such that the arrest radius can be approximated as

$$R_{\tilde{m},a} \approx 0.5218 \frac{E^{1/13} V_o^{5/13}}{C^{2/13} \mu^{1/13}} \text{ for } \mathcal{C}_s \lesssim 0.25. \quad (22)$$

We will refer to this estimate of the arrest radius as the “early shut-in” approximation (where early refers to small \mathcal{C}_s). On the other hand, for values of \mathcal{C}_s larger than 2.5, the arrest radius is the radius at shut-in which follows the viscosity/leak-off regime (\tilde{M}) constant injection solution (Madyarova, 2003; Detournay, 2016; Dontsov, 2016), as can be seen in Fig. 4. We refer to this limit as the “late shut-in” (large \mathcal{C}_s) solution hereafter. We can infer that the fracture will immediately stop its propagation somewhat for \mathcal{C}_s between 0.25 and 2.5. We estimate the critical dimensionless leak-off coefficient

at shut-in $\mathcal{C}_{s,c}$ for immediate arrest from our simulations as $\mathcal{C}_{s,c} \approx 0.53 \pm 0.05$ by again using the criterion $R_s/R_a(\mathcal{C}_s) \geq 0.975$ for immediate arrest (red dashed line in Fig. 4). It is important to note that contrary to the impermeable case, the arrest radius is not uniquely defined for all \mathcal{C}_s . For small \mathcal{C}_s (below 0.25), the arrest radius is constant but not for larger values. Immediate arrest occurs for $\mathcal{C}_{s,c} \approx 0.53$ and the arrest radius for \mathcal{C}_s larger than $\mathcal{C}_{s,c}$ coincides with the shut-in radius which can be well approximated by the viscosity/leak-off dominated injection solution (within a few percent for $\mathcal{C}_s > 4$).

We now turn to quantify the amount of propagation after the end of the injection. As expected, the propagation in the zero toughness case follows the known solutions during injection (Savitski and Detournay, 2002; Madyarova, 2003; Dontsov, 2016) ($t/t_s < 1$ in Fig. 5 left, blue (storage), and light blue (leak-off) dashed lines). One can observe from Fig. 5a that the propagation after shut-in ($t/t_s > 1$) for the “early shut-in” cases ($\mathcal{C}_s \lesssim 0.25$) follows the viscosity/storage pulse solution (developed in section 3.2) at intermediate times before the final arrest. We can thus estimate the amount of propagation after shut-in for values of $\mathcal{C}_s \lesssim 0.25$ by comparing the radius at shut-in (evaluated from the viscosity storage injection solution Madyarova, 2003; Dontsov, 2016) with the “early shut-in” arrest radius (22):

$$\frac{R_{\tilde{m},a}}{R_s} \approx \frac{0.5218 \left(\frac{E^{1/13} V_o^{5/13}}{C^{2/13} \mu^{1/13}} \right)}{0.6978 \left(\frac{E^{1/9} Q_0^{1/3} t_s^{4/9}}{\mu^{1/9}} \right)} \approx 0.75 \mathcal{C}_s^{-2/13}. \quad (23)$$

We recall that the prefactor of 0.5218 is obtained by fitting our numerical results such that Eq. (23) is also an approximation. Such an approximation compares very well with our numerical results up to $\mathcal{C}_s \lesssim 0.25$ as can be seen in Fig. 6a. The power-law dependence of the ratio between the time of arrest and the shut-in time can be similarly derived from (20) as $t_a/t_s \propto \mathcal{C}_s^{-18/13}$. Such a dependence captures well our numerical results as displayed in Fig. 6b where a linear regression was performed to obtain a prefactor of 0.044 (Fig. 6b). The time of arrest can thus be estimated for small \mathcal{C}_s as:

$$\frac{t_a}{t_s} \approx 0.044 \mathcal{C}_s^{-18/13} \text{ for } \mathcal{C}_s \lesssim 0.25.$$

The effect of leak-off on the arrest can also be grasped by looking at the evolution of fracturing efficiency η , defined as the ratio between the fracture volume V_f and the injected volume V_{inj} :

$$\eta = \frac{V_f}{V_{inj}}, \quad \text{with : } V_{inj} = \begin{cases} Q_0 t & \text{for } t < t_s \\ V_o & \text{for } t \geq t_s \end{cases} \quad (24)$$

For example, an efficiency of $\eta = 0.5$ indicates that half of the fluid injected remains inside the fracture, while the rest has leaked to the surrounding rock. The dimensionless leak-off coefficient is linked in a non-linear way to fracturing efficiency, and both help to characterize the propagation and arrest of the fracture after shut-in. From Fig. 5b, we can relate the critical value of dimensionless leak-off coefficient at shut-in $\mathcal{C}_{s,c} \approx 0.53$, to a unique critical value of fracturing efficiency of $\eta_c = \eta(\mathcal{C}_m(t_s) = \mathcal{C}_{s,c}) \approx 0.44$. This allows us to estimate the loss of fluid necessary to stop instantaneously the fracture from propagating at shut-in. In other words, from the moment on that a bit more than half of the total amount of fluid injected is lost due to leak-off, the fracture will stop immediately upon shut-in. Finally, we are able to assess the possibility of post-injection propagation via the fracturing efficiency η , by observing Fig. 5b. One can see that for \mathcal{C}_s smaller than 0.25 (for which the “early shut-in” approximation is valid), the arrest seems to occur when the fracturing efficiency falls to a common value of 0.68 irrespective of \mathcal{C}_s . From this, we infer that the fracturing efficiency at shut-in $\eta_s = \eta(\mathcal{C}_s)$ indicates the potential of post-injection propagation, as follow:

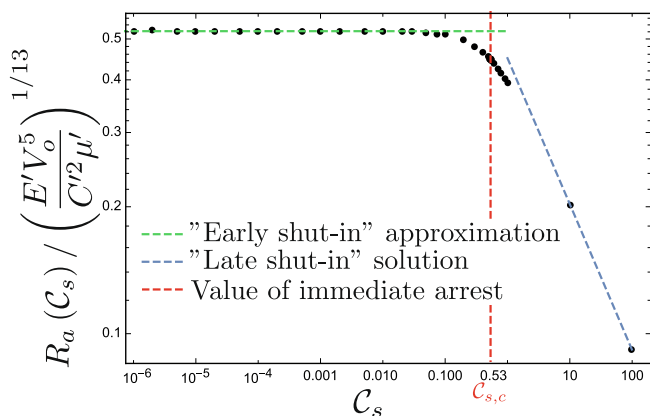


Fig. 4. Numerical evaluation of the arrest radius for different values of \mathcal{C}_s in the zero toughness case. The early shut-in approximation is given in Eq. (21) with its prefactor obtained by regression of these numerical results. The late shut-in solution corresponds to the radius at shut-in given by the viscosity/leak-off propagation solution of Madyarova (2003).

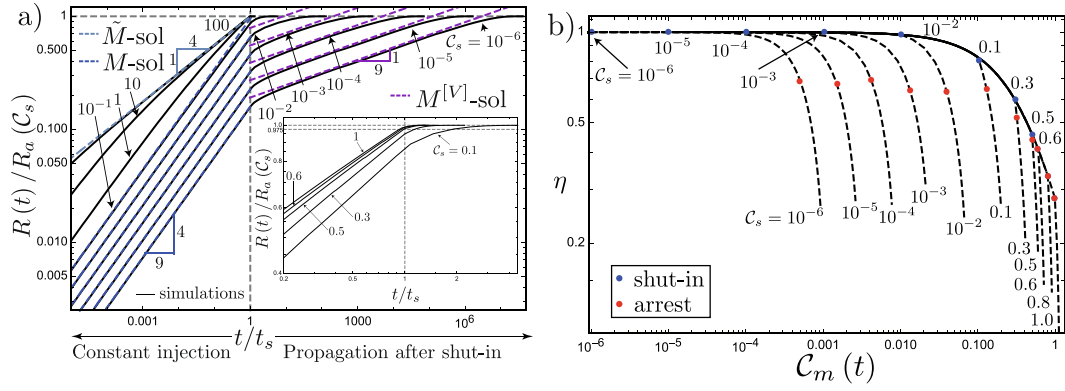


Fig. 5. a) Normalized fracture radius in function of characteristic shut-in time t/t_s . Numerical (and semi-analytical) predictions of fracture radius scaled by the arrest radius $R_a(C_s)$ for various values of shut-in leak-off coefficient C_s (from 10^{-6} to 10^2). b) Fracturing efficiency as a function of dimensionless leak-off coefficient $C_m(t) = C_s \times (t/t_s)^{7/18}$. Black dashed lines correspond to numerical simulations with different values of shut-in leak-off coefficient C_s . Blue dots mark the moment of shut-in, and red dots mark the moment of fracture arrest.

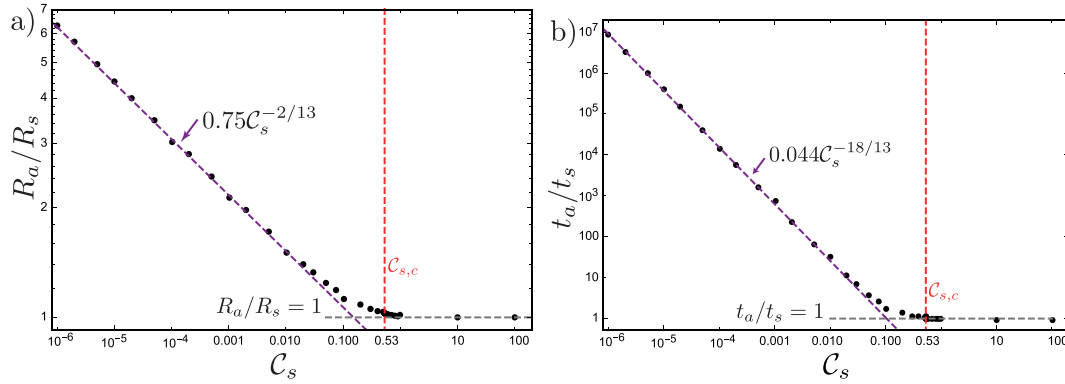


Fig. 6. Characteristical values of post-injection propagation in function of shut-in leak-off coefficient C_s . a) Overshoot of a radial fracture in the case of zero toughness. b) Time of persistent propagation of a radial fracture in the case of zero toughness.

$$\begin{aligned}
 \eta_s > \eta_a = 0.68 & \quad \text{post-shut-in propagation,} \\
 \eta_c \leq \eta_s < \eta_a & \quad \text{negligible post-shut-in propagation,} \\
 \eta_s < \eta_c = 0.44 & \quad \text{immediate arrest.}
 \end{aligned} \quad (25)$$

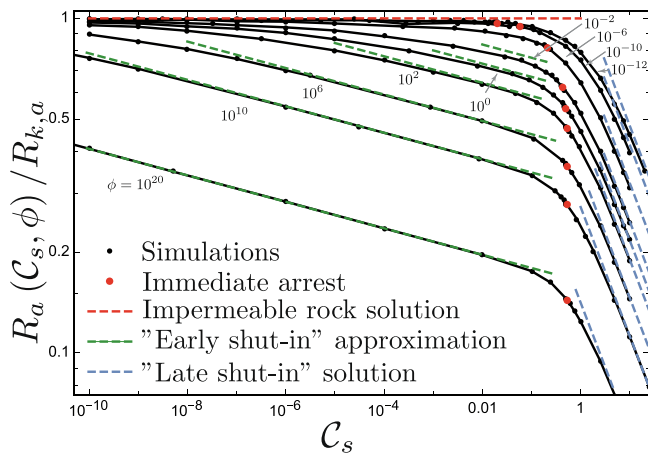


Fig. 7. Normalized arrest radius $R_a/R_{k,a}$ in function of the dimensionless leak-off coefficient at shut-in C_s for different values of the trajectory parameter $\phi = C_s^4/\mathcal{H}_s^{14}$. Black dots are simulations results, red dots correspond to the critical value above which the arrest is immediate upon shut-in. The red dashed line is the zero leak-off arrest radius, green dashed lines are the "early shut-in" arrest radius approximation, and light blue lines the late shut-in solution.

4.2. General case

When accounting for both finite toughness and leak-off, the solution now depends on the corresponding dimensionless parameters at shut-in (\mathcal{H}_s and C_s). The two are directly related by the trajectory parameter $\phi = C_s^4/\mathcal{H}_s^{14}$. We alternatively use \mathcal{H}_s (or C_s) and ϕ to characterize the arrest radius and post-shut-in propagation.

We numerically evaluate the radius of arrest by performing a large number of simulations (≈ 450 simulations) for various values of the trajectory parameter $\phi = C_s^4/\mathcal{H}_s^{14}$ ranging from 10^{-12} to 10^{20} . The results are displayed in Fig. 7 together with limiting solutions in the impermeable and zero toughness cases. First of all, we observe that for $C_s > 2.5$, the arrest radius is immediate independent of the value of \mathcal{H}_s (i.e. independent of ϕ): one retrieves the "late shut-in" arrest radius (viscosity/leak-off regime injection solution Madyarova, 2003; Dontsov, 2016). For $\phi > 1$, the arrest radius follows the early shut-in approximation (Eq. (22)) for intermediate values of C_s . For a given value of ϕ , the arrest radius tends to the impermeable arrest radius $R_{k,a}$ (Eq. (14a)) when C_s vanishes. Finally, the impermeable arrest radius $R_{k,a}$ (Eq. (14a)) is already a good estimate for values of $C_s \leq 10^{-2}$ when $\mathcal{H}_s \lesssim 0.8$ (i.e. when $\phi \leq 10^{-6}$).

From this series of simulations as well as the limits for arrest obtained in the impermeable ($\mathcal{H}_{s,c} \approx 2.5$) and zero-toughness case ($C_{s,c} \approx 0.53$), we can delineate in the (\mathcal{H}_s, C_s) phase space, the regions where post-shut-in growth does or does not occur.

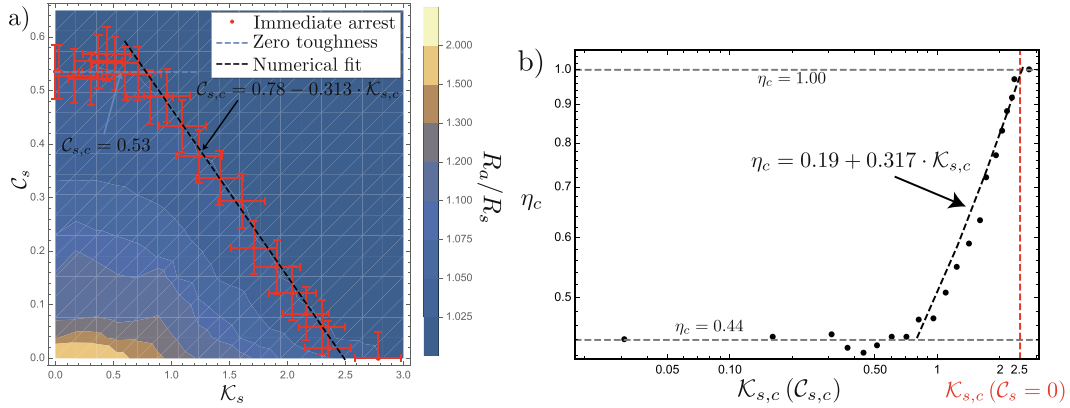


Fig. 8. a) Contour plot of propagation after shut-in. Red dots are the numerically evaluated values of immediate arrest at shut-in, the light blue dashed line gives the critical dimensionless leak-off coefficient in the zero-toughness case ($\mathcal{C}_{s,c} \approx 0.53 \pm 0.05$) and the black dashed line is a numerical fit for intermediate values. b) Critical fracturing efficiency in function of the critical dimensionless toughness at shut-in.

Fig. 8a displays the ratio between the final arrest radius and the shut-in radius, and red dots correspond to the boundary for immediate arrest (estimated numerically following the same threshold of 2.5% then in the limiting zero-toughness and impermeable cases). From these results, we can further provide the following approximation for this boundary for immediate arrest:

$$\begin{aligned} \mathcal{C}_{s,c} &\approx 0.53 & \mathcal{K}_{s,c} < 0.8 \\ \mathcal{C}_{s,c}(\mathcal{K}_{s,c}) &\approx 0.78 - 0.313 \cdot \mathcal{K}_{s,c} & \text{for } \mathcal{K}_{s,c} \in [0.8, 2.5]. \end{aligned} \quad (26)$$

where the limit of $\mathcal{K}_{s,c} = 2.5$ is retrieved for $\mathcal{C}_s = 0$. Such a boundary is approximate with a resolution of about 3 to 5 percent accounting for our numerical errors and our sampling of the $(\mathcal{K}_s, \mathcal{C}_s)$ phase space.

Using Fig. 5b the value of $\mathcal{K}_{s,c}$ can be used to get an equivalent value of the fracturing efficiency $\eta_c = \eta_s(\mathcal{K}_{s,c})$. As expected, the critical efficiency tends towards the zero toughness limit of $\eta_c = 0.44$ when $\mathcal{K}_{s,c}$ gets below 0.8. A critical fracturing efficiency of 1 is reached for $\mathcal{K}_{s,c} = 2.5$ which corresponds to the critical shut-in toughness in the impermeable case. The evolution of the critical fracturing efficiency (upon which arrest is immediate at shut-in) as a function of $\mathcal{K}_{s,c}$ can be approximated in a piecewise linear manner as follow:

$$\begin{aligned} \eta_c &\approx 0.44 & \mathcal{K}_{s,c} < 0.8 \\ \eta_c &\approx 0.190 + 0.317 \cdot \mathcal{K}_{s,c} & \text{for } \mathcal{K}_{s,c} \in [0.8, 2.5] \\ \eta_c &= 1.00 & \mathcal{K}_{s,c} = 2.5. \end{aligned} \quad (27)$$

Similarly than for the limiting impermeable and zero-toughness cases, we quantify the post-shut-in propagation in terms of propagated distance and time of arrest. Fig. 9a and b display respectively the ratio of the final arrest radius over the shut-in radius and the time of final arrest over the shut-in time. We observe that as the trajectory parameter ϕ / leak-off increases (\mathcal{C}_s increases at constant \mathcal{K}_s), the arrest time and corresponding radius decrease. They depart from the impermeable solution (14a) and switch to the early shut-in approximation (22) for intermediate values of \mathcal{K}_s . The limit of immediate arrest is clearly visible in those plots: it corresponds to the lowest value of \mathcal{K}_s for which $R_a/R_s = t_a/t_s = 1$ and is highlighted by a red dot for a given ϕ . From Fig. 9a and b, we can see that the impermeable solution provide a good estimate of the post-injection propagation and time of arrest for values of $\phi \leq 10^{-6}$ for all \mathcal{K}_s . For values of $\phi > 10^{-6}$, the impermeable solution is valid up to a given value of \mathcal{K}_s , which decreases as ϕ increases. For a given ϕ , the zero-toughness estimate is valid in the intermediate range of \mathcal{K}_s , nearly up to $\mathcal{K}_{s,c}(\mathcal{C}_{s,c})$. These plots provide a simple and efficient way to quickly estimate the amount of propagation post-shut-in as a function of \mathcal{K}_s and \mathcal{C}_s ($\phi = \mathcal{C}_s^4 / \mathcal{K}_s^{14}$).

5. Discussions

5.1. Orders of magnitude for industrial applications

The results of the previous sections are notably applicable to industrial applications related to well stimulation (Economides

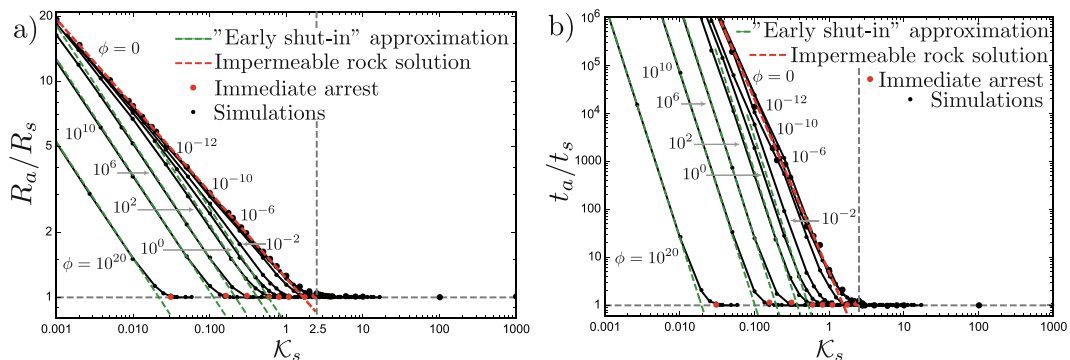


Fig. 9. Propagation post-shut-in (final arrest radius divided by the radius at shut-in) in the general case as a function of the dimensionless toughness at shut-in \mathcal{K}_s for different values of the trajectory parameter $\phi = \mathcal{C}_s^4 / \mathcal{K}_s^{14}$. The red dashed line corresponds to the impermeable medium case, while the green dashed lines represent the early shut-in leak-off approximation. Red dots indicate the limit of immediate arrest, and black dots are numerical simulations.

Table 2

Characteristic values of industrial HF applications for a so-called single entry treatment (propagation of a single hydraulic fracture).

| Cases | μ [Pa · s] | Q_o [m ³ /s] | t_s [s] | V_o [m ³] | E [GPa] | ν [–] | K_{Ic} [MPa · √m] |
|--|-------------------|---------------------------|-----------|-------------------------|-----------|-----------|---------------------|
| (1) Gel injection into a sandstone | $5 \cdot 10^{-3}$ | 0.05 | 2/700 | 135 | 20 | 0.25 | 1.5 |
| (2) Slickwater injection into a mudstone | 1 | 0.01 | 2/700 | 27 | 30 | 0.25 | 1.0 |

and Nolte, 2000; Detournay, 2016). Hydraulic fracturing treatments normally consist of a series of injections under a constant rate propagating fluid-driven fractures in a rock formation. These fractures are then filled by a proppant bearing fluid (keeping the fracture open/propped) to enhance the permeability of such sand- and mudstone reservoirs. We focus on the case of a single entry treatment where a single hydraulic fracture is propagated. A broad range of fluids have been designed for these treatments, linear or cross-linked gels as well as slickwater are commonly used (Barbati et al., 2016; Lecampion and Zia, 2019). To assess the order of magnitude of post-injection propagation, we illustrate our findings with the two examples listed in Table 2.

We assume two values for the leak-off parameter, $C' = 10^{-6}$ and $C' = 10^{-10}$ (see discussion in Lecampion et al. (2018) for an estimation of the range of leak-off properties). The large leak-off parameter is likely to occur in porous sandstones, whereas the small value is more likely for tight mudstones (although the coefficient is also dependent on fracturing fluid type). We will, however, apply both coefficients to case (1) and (2) as to assess the entire range of possible propagation after shut-in.

The four possible combinations (cases (1) and (2) of Table 2 with the two values of C') result in a large range of trajectory parameters $\phi \in [10^{-25}, 5 \cdot 10^1]$. The value of the dimensionless shut-in toughness in these cases varies within one order of magnitude ($\mathcal{H}_s^{(1)} = 1.44$ and $\mathcal{H}_s^{(2)} = 0.21$) and the dimensionless shut-in leak-off coefficient from $\mathcal{G}_s = 10^{-6}$ to $\mathcal{G}_s = 0.022$. We discuss case (1) combined with the higher leak-off parameter (minimum propagation after shut-in) and case (2) with the low leak-off coefficient (maximum propagation after shut-in). The results of all four combinations are listed in Table 3.

The slickwater injection into sandstone with a large leak-off coefficient ($C' = 10^{-6}$) results in a dimensionless shut-in toughness of $\mathcal{H}_s = 1.44$, a shut-in leak-off parameter of $\mathcal{G}_s = 0.022$ and a trajectory parameter $\phi = 1.5 \cdot 10^{-9}$. Following Fig. 7, we estimate the radius of arrest as approximately $0.95 \cdot R_{k,a} \approx 166$ [m] (where $R_{k,a}$ is given by Eq. (14a)). We derive the ratio between arrest and shut-in radius from Fig. 9a as $R_a/R_s \approx 1.10$ corresponding to a propagation after shut-in of about 10%. From Fig. 7, we estimate that $t_a/t_s \approx 2.5$ leading to an elapsed time between shut-in and arrest of about $t_a - t_s \approx 1.5 t_s \approx 4050$ [s].

For the second case with a small leak-off coefficient ($C' = 10^{-10}$), the dimensionless parameters at shut-in are now $\mathcal{H}_s = 0.21$, $\mathcal{G}_s = 1.2 \cdot 10^{-6}$, corresponding to $\phi = 5.5 \cdot 10^{-15}$. This allows us to estimate the arrest radius using Eq. (14a) yielding a value of $R_a = 127$ [m]. It is further possible to estimate the radius at shut-in with the viscous propagation solution of Savitski and

Detournay (2002) $R_s = 56$ [m] giving us a precise estimation of the propagation after shut-in of $R_a/R_s \approx 2.27$. The arrest radius is thus more than twice the radius at shut-in and growth after shut-in accounts for another 127% of the growth during the injection ($R_a - R_s \approx 1.27 R_s$). The ratio between the arrest and the shut-in time is very large and estimated as $t_a/t_s \approx 5.0 \mathcal{H}_s^{-18/5} \approx 1272$, leading to an arrest time of $t_a \approx 3.43 \cdot 10^6$ [s] ≈ 40 [d].

5.2. Orders of magnitude for a magmatic pulse release

Natural hydraulic fractures can occur via magmatic intrusion through the lithosphere. We illustrate the impact of the post-injection propagation of a dike assuming a strictly impermeable medium. We neglect buoyant forces for simplicity and assume a Newtonian rheology for the magma. We use the material parameters specified in Table 4, where we estimate the volume V_o as a mean volume for dike intrusions at the Piton de la Fournaise volcano on La Réunion between 1998 and 2016 (Froger et al., 2004; Fukushima et al., 2010; Smittarello et al., 2019). Estimation of the injection time is difficult, but measurements of mean magma flow rates and injection durations allow to define a range from 0.1 to 10 [m³s⁻¹] (Fukushima et al., 2005, 2010), which allows us to approximate the injection duration. The viscosity of the basaltic magma at Piton de la Fournaise is evaluated by Villeneuve et al. (2008) and expected to range between 300 [Pa · s] and 100 [Pa · s] at around $1100 - 1150$ [°C] Celsius (temperature observed by Fukushima et al. (2010)). We use an average value of 200 [Pa · s] here. This leads to values of the shut-in toughness of $\mathcal{H}_s^{(3)} \approx 0.044$, and $\mathcal{H}_s^{(4)} \approx 0.16$ allowing to estimate the shut-in radius via the storage/viscosity dominated M -solution (Savitski and Detournay, 2002) and the arrest radius from Eq. (14a). The results are summarized in Table 5 and indicate a significant propagation after shut-in ranging from 156% to 327% of the shut-in radius. We observe that the propagation time post-shut-in is very long such that cooling of the magma will likely reduce the post-release propagation significantly. Such an effect of cooling could be at first order modeled in a similar manner than fluid-leak-off as it is dominated by thermal conduction between the dike and the surrounding rock. Another very important point is that buoyant forces can not be neglected in this case, such that the fracture will likely deviate from the radial shape and elongate to form a three-dimensional buoyancy-driven dike (Rivalta et al., 2015). The characteristic lengthscale for buoyancy-driven propagation is given as $L_b = (K'/\Delta\rho g)^{2/3}$ (Lister and Kerr, 1991). Taking an average rock density of $\rho_s = 2900$ [kg/m³] and the density of the basaltic magma at Piton de la Fournaise from Villeneuve et al. (2008) as

Table 3

Resulting dimensionless parameters, arrest and shut-in radius as well as post-injection propagation and elapsed time between shut-in and arrest.

| Cases | ϕ [–] | \mathcal{G}_s [–] | \mathcal{H}_s [–] | R_a [m] | R_s [m] | R_a/R_s | t_a/t_s |
|---|-------------------------|------------------------|---------------------|---------------|---------------|----------------|----------------|
| (1) Gel injection into a sandstone with $C' = 10^{-6}$ | $\mathcal{O}(10^{-9})$ | 0.022 | 1.44 | ≈ 166 | ≈ 151 | ≈ 1.10 | ≈ 2.5 |
| (1) Gel injection into a sandstone with $C' = 10^{-10}$ | $\mathcal{O}(10^{-25})$ | $\mathcal{O}(10^{-6})$ | 1.44 | 175 | ≈ 159 | ≈ 1.10 | ≈ 2.5 |
| (2) Slickwater injection into a mudstone with $C' = 10^{-6}$ | 54.7 | 0.012 | 0.21 | ≈ 82 | 56 | ≈ 1.47 | ≈ 50 |
| (2) Slickwater injection into a mudstone with $C' = 10^{-10}$ | $\mathcal{O}(10^{-15})$ | $\mathcal{O}(10^{-6})$ | 0.21 | 127 | 56 | 2.27 | ≈ 1272 |

Table 4

Estimated values for the injection of magma neglecting buoyant forces.

| Cases | μ [Pa · s] | V_o [m ³] | Q [m ³ /s] | t_s | E [GPa] | ν [–] | K_{Ic} [MPa · √m] |
|------------------------------------|----------------|-------------------------|-------------------------|------------------|-----------|-----------|---------------------|
| (3) Short injection with high rate | 200 | $5 \cdot 10^5$ | 10 | ≈ 14 [h] | 20 | 0.2 | 1.5 |
| (4) Long injection with low rate | 200 | $5 \cdot 10^5$ | 0.1 | ≈ 60 [d] | 20 | 0.2 | 1.5 |

Table 5

Resulting fracture dimensions and propagation post-injection for a magmatic release (not accounting for buoyancy forces).

| Cases | $R_{k,a}$ [km] | R_s [km] | R_a/R_s | t_a/t_s |
|------------------------------------|----------------|------------|----------------|--------------------------|
| (3) Short injection with high rate | 4.64 | 1.09 | ≈ 4.27 | $\approx 3.8 \cdot 10^6$ |
| (4) Longer injection with low rate | 4.64 | 1.81 | ≈ 2.56 | $\approx 3.8 \cdot 10^3$ |

$\rho_f \approx 2800$ [kg/m³], the characteristic lengthscale for buoyant propagation is $L_b \approx 288$ [m], which is significantly smaller than the arrest radius $R_{k,a} = 4.64$ [km]. This clearly indicates that buoyancy forces are of first-order in that particular case such that most likely they take over and elongate the fracture before it reaches the radial arrest radius. The further investigation of the conditions for the transition from a radial to a buoyant dike after a given volume release is out of the scope of this contribution, one can nevertheless anticipate that such a transition will be grasped by the ratio between the arrest radius and the buoyancy lengthscale.

5.3. Importance of subcritical crack growth

Stable crack propagation can occur even when $K_{I,min} < K_I < K_{Ic}$ (where $K_{I,min}$ is a material-dependent limit below which no growth is observed), albeit at small velocities (Atkinson, 1984, 1987). An empirical relation between fracture velocity dR/dt and the ratio K_I/K_{Ic} is known to reproduce well experimental observations in this sub-critical regime (Charles, 1958a,b)

$$\frac{dR}{dt} = A \left(\frac{K_I}{K_{Ic}} \right)^n \quad (28)$$

where A and n are experimentally determined parameters. Subcritical crack growth has been observed in laboratory HF experiments (Lu et al., 2017; Winner et al., 2018) when a constant fluid pressure below the critical value required for toughness dominated crack growth is applied. We briefly discuss the implications of additional sub-critical growth even after the arrest radius estimated from linear elastic fracture mechanics has been reached. We restrict ourselves to the impermeable case for simplicity. The effect will be maximal for that case as toughness is the sole arresting mechanism.

For a toughness dominated case, the fluid pressure is spatially uniform in the fracture, fracture width is given by (12), the mode I stress intensity factor K_I remains given by (13) while the fracture volume is equal to V_o . Replacing the classical LEFM propagation condition $K_I = K_{Ic}$ by the sub-critical crack law (28) in this set of equations, one obtains the following differential equation for the radius evolution

$$\frac{dR}{dt} = A' \left(\frac{E'V_o}{K_{Ic}} \right)^n R^{-5n/2} \quad (29)$$

with $A' = A \times (3/8\sqrt{\pi})^n$. We are interested to gauge sub-critical crack growth beyond the arrest provided by linear elastic fracture mechanics. We thus use the LEFM radius of arrest given by Eq. (14a) as the initial condition to solve (29). We obtain the following crack radius evolution

$$R(t - t_{k,a}) = \left(AR_{k,a}^{5n/2} \times \left(1 + \frac{5n}{2} \right) \times (t - t_{k,a}) \right)^{\frac{2}{2+5n}} \quad (30)$$

Eq. (30) is valid when $t - t_{k,a} > 2R_{k,a}/(2A + 5An)$. Assuming common orders of magnitudes for $R_{k,a} = \mathcal{O}(10^1 - 10^3)$ [m], $A = \mathcal{O}(10^3)$ [m/s], and $n = \mathcal{O}(10^1 - 10^2)$ (Lu et al., 2017), this temporal limit is of the order $t - t_{k,a} > \mathcal{O}(10^{-4} - 10^{-1})$ [s].

The criterion for complete fracture arrest is reached when K_I drops below the minimum value $K_{I,min}$ which is in the order of $K_{I,min} = K_{Ic}/10$ (Lu et al., 2017). This lower limit allows us to estimate the time when the stress intensity factor drops below $K_{I,min}$ and sub-critical propagation comes to a halt:

$$t_{sc,a} - t_{k,a} = \frac{2R_{k,a} \left(10^{\frac{2}{2+5n}} - 1 \right)}{A(2 + 5n)} \quad (31)$$

where $t_{sc,a}$ is the arrest time of sub-critical propagation. The radius (30) at that time corresponds to the final arresting radius including sub-critical growth:

$$R_{sc,a} = \left(10^{\frac{2}{2+5n}} - 1 \right)^{\frac{2}{2+5n}} R_{k,a} \approx 10^{2/5} R_{k,a} \approx 2.51 R_{k,a} \quad (32)$$

For the range of n typical for rocks ($n \in [10, 200]$, Lu et al. (2017)), this subcritical arrest radius is interestingly reduced to a constant amount of the arrest radius $R_{k,a}$. We thus see that sub-critical crack growth adds a significant amount of propagation, about 2.5 times the LEFM arrest radius. Subcritical fracture propagation is thus likely an important mechanism in the impermeable case. It needs to be pointed out that the time during which the fracture grows subcritical is very large (the minimum arrest time is $\min(t_{sc,a} - t_{k,a}) = \mathcal{O}(10^7)$ [s] for common values of $R_{k,a}$, n and A). The influence of leak-off will, of course, decrease the impact of sub-critical crack growth as arrest will likely occur first due to leak-off. The case of an impermeable medium corresponds thus to the maximum upper bound for the post shut-in sub-critical growth. We leave the quantitative details of the competition between a small amount of leak-off and sub-critical crack growth to additional studies.

6. Conclusions

We have quantified numerically the propagation of a hydraulic fracture after the end of the injection in an isotropic, homogeneous, elastic medium driven by a Newtonian fluid under the assumption of Carter leak-off.

For an impermeable medium, the arrest radius R_a corresponds to the solution of a quasi-static crack at equilibrium ($K_I = K_{Ic}$) under a uniform net loading with a volume equal to the injected one. The arrest radius does not depend on any dimensionless number and is independent of the injection history in that case. For a

permeable medium, the arrest radius is independent of the injection history only for small values of the dimensionless leak-off coefficient at shut-in $\mathcal{C}_s \lesssim 0.25$ and reduces for increasing values of \mathcal{C}_s . Based on scaling arguments and numerical simulations, we obtain an approximation (22) of the arrest radius in the zero-toughness case valid for $\mathcal{C}_s \lesssim 0.25$. The arrest radius for $\mathcal{C}_s > 2.5$ and $\mathcal{K}_s = 0$ (“late shut-in” solution) corresponds to the viscosity/leak-off dominated solution for a constant injection rate (Madyarova, 2003). In the general case of finite toughness and leak-off, the solution of the arrest radius for an impermeable rock is a good estimate for small $\phi = \mathcal{C}_s^4 / \mathcal{K}_s^{14}$ / leak-off, while the “early shut-in” approximation is valid for large ϕ /leak-off. In any case, for $\mathcal{C}_s > 2.5$, the arrest radius follows the “late shut-in” solution.

The arrest is immediate upon shut-in if the dimensionless toughness \mathcal{K}_s at shut-in is larger than a critical value $\mathcal{K}_{s,c} = 2.5$ in the impermeable case. Leak-off reduces the value of this critical dimensionless toughness for immediate arrest. In the zero-toughness case, the arrest is immediate for $\mathcal{C}_s \geq \mathcal{C}_{s,c} \approx 0.53$, where $\mathcal{C}_{s,c}$ is the critical value of a dimensionless coefficient at shut-in. The immediate arrest for finite toughness and leak-off can be approximated as $\mathcal{C}_{s,c} \approx 0.53$ for $\mathcal{K}_{s,c} < 0.8$ and $\mathcal{C}_{s,c}(\mathcal{K}_{s,c}) \approx 0.78 - 0.313 \cdot \mathcal{K}_{s,c}$ for $\mathcal{K}_{s,c} > 0.8$.

When $\mathcal{K}_s < \mathcal{K}_{s,c}$ and $\mathcal{C}_s < \mathcal{C}_{s,c}(\mathcal{K}_{s,c})$, post-injection propagation does occur. For $\phi < 10^{-2}$ and $\mathcal{K}_s < 1$, the ratio between the arrest and shut-in radius is given by $R_a/R_s \approx 1.23 \mathcal{K}_s^{-2/5}$ (Eq. (18)) which corresponds to the impermeable limit. For $\phi > 1$, we still observe $R_a/R_s \approx 1.23 \mathcal{K}_s^{-2/5}$ for small values of \mathcal{K}_s while the early shut-in approximation $R_a/R_s \approx 0.75 \mathcal{K}_s^{-7/13} \phi^{-1/26}$ is valid for intermediate values of \mathcal{K}_s smaller than the critical value $\mathcal{K}_{s,c}(\mathcal{C}_{s,c})$. For small values of dimensionless toughness and leak-off coefficient at shut-in ($\mathcal{K}_s \leq 0.1$ and $\mathcal{C}_s < 10^{-2}$), the post-shut-in growth is well captured by an intermediate self-similar viscosity-storage pulse solution. This self-similar solution can be accurately obtained numerically using a collocation method based on Gauss–Chebyshev quadrature and barycentric differentiation and interpolation (see Appendix B for details). The fracture radius evolves as $R(t) \approx 0.836 \frac{P^{1/9} V_f^{1/3} t^{1/9}}{\mu^{1/9}}$ in that viscosity-storage pulse regime where the fracture velocity decreases much faster ($\frac{dR}{dt} \propto t^{-8/9}$) than during continuous injection ($\frac{dR}{dt} \propto t^{-5/9}$).

For realistic parameters, fracture propagation after shut-in may be of the same order as the propagation during the injection. Subcritical crack growth can further extend this post-injection propagation (we provide an upper limit for this mechanism). The time of arrest can be orders of magnitude larger than the shut-in time. As shown, post-shut-in growth is very sensitive to the amount of leak-off. It is clear that the estimate obtained here under the assumption of Carter leak-off has to be taken with caution. Indeed, Carter's leak-off is by essence pressure independent: it assumes a constant over-pressure in the fracture which results in the $1/\sqrt{t}$ behavior. This assumption is clearly questionable at large time after the end of the injection. Accounting for pressure-dependent leak-off (Kanin et al., 2020) would certainly modify the estimation of arrest in the large leak-off cases. Similarly, poroelastic effects will promote an earlier arrest due to the back-stress associated with the increased pore-pressure around the fracture (Detournay and Cheng, 1991). Another factor possibly reducing the fracture extent in industrial applications is the presence of proppant. The fracture may close on the proppant thus modifying the arrest. We thus see that the estimates we have derived here provide an upper bound for the post-injection growth of hydraulic fractures. The impact of the previously mentioned effects (pressure dependent leak-off, poroelasticity, proppant) favoring an earlier fracture arrest after the end of the injection remains to be quantified in detail.

Funding

This research was funded by the Swiss National Science Foundation (Grant #192237).

CRediT authorship contribution statement

Andreas Möri: Conceptualization, Methodology, Formal analysis, Investigation, Software, Validation, Visualization, Writing - original draft. **Brice Lecampion:** Conceptualization, Methodology, Formal analysis, Supervision, Funding acquisition, Writing - review & editing.

Declaration of Competing Interest

The authors declare that they have no known competing financial interests or personal relationships that could have appeared to influence the work reported in this paper.

Appendix A. Energy budget of a radial hydraulic fracture

We briefly recall the energy budget of a radial hydraulic fracture to highlight the energy split after shut-in. The energy balance for the elastic material under the assumption of linear elastic fracture mechanics and a propagating radial fracture reads (Rice, 1968):

$$2\pi R G_c \frac{dR}{dt} = \int_0^R \frac{1}{2} \left(p(r, t) \frac{\partial w(r, t)}{\partial t} - w(r, t) \frac{\partial p(r, t)}{\partial t} \right) 2\pi r dr \quad (33)$$

while the energy budget of the lubrication flow in a radial hydraulic fracture is given by (Lecampion and Detournay, 2007):

$$\begin{aligned} & \int_0^R p(r, t) \frac{\partial w(r, t)}{\partial t} 2\pi r dr + \int_0^R \frac{\mu'}{w(r, t)} V_f^2(r, t) 2\pi r dr \\ & + \int_0^R v_L(r, t) p(r, t) 2\pi r dr \\ & = Q_o(t) p(0, t). \end{aligned} \quad (34)$$

where $V_f = q/w$ is the width-average fluid velocity inside the fracture and v_L is the leak off rate $v_L = C'/\sqrt{t - t_o(r)}$. Summing up the two previous equations, and integrating in time from the shut-in time t_s to the current time $t \geq t_s$, one obtains the following global energy balance after shut-in (where $Q_o = 0$ and such is the input energy):

$$\begin{aligned} & \underbrace{G_c \pi (R^2(t) - R^2(t_s))}_{\text{creation of new surfaces}} \\ & + \underbrace{\int_{t_s}^t \int_0^R \frac{1}{2} \left(p(r, t) \frac{\partial w(r, t)}{\partial t} + w(r, t) \frac{\partial p(r, t)}{\partial t} \right) 2\pi r dr}_{\text{stored elastic energy}} \\ & + \underbrace{\int_{t_s}^t \int_0^R \frac{\mu'}{w(r, t)} V_f^2(r, t) 2\pi r dr}_{\text{viscous flow}} + \underbrace{\int_{t_s}^t \int_0^R v_L(r, t) p(r, t) 2\pi r dr}_{\text{leak-off}} \\ & = 0. \end{aligned} \quad (35)$$

We clearly see that the terms associated with viscous flow inside the fracture and leak-off (under the assumption of Carter's leak-off) are always positive. Similarly, the energy spent in the creation of new fracture surface is always positive as $R(t) \geq R(t_s)$. On the contrary, after shut-in, the width and pressure decreases: $\partial w(r, t)/\partial t < 0$ and $\partial p(r, t)/\partial t < 0$. The available elastic stored energy term decreases with time thus ultimately leading to arrest. The fracture arrests when an equilibrium is reached between frac-

ture energy, leak-off and viscous flow, when the available stored energy goes to zero as $\partial w(r, t)/\partial t = \partial p(r, t)/\partial t = 0$.

Appendix B. Viscous pulse solution

The self-similar solution of a viscosity-dominated radial hydraulic fracture after shut-in (after a pulse injection) is solved numerically. Following the techniques described in Liu et al. (2019) and Viesca and Garagash (2018), we combined Gauss–Chebyshev quadrature with Barycentric Lagrange interpolation and differentiation. The problem is thus reduced to a system of non-linear equations which can be solved by root finding. We recall here the most important points and refer to Viesca and Garagash (2018) for a detailed description of this spatial discretization method and to Liu et al. (2019) for its application to finite hydraulic fractures under constant injection.

B.1. Gauss–Chebyshev quadrature

Gauss–Chebyshev quadrature is a well-known technique for the solution of elastic boundary integral equations arising in fracture problems (Erdogan et al., 1973). The quadrature uses two sets of nodes, a primary one $\mathbf{s} = \{s_j\}$ with $j = 1, \dots, n$ and a complementary set $\mathbf{z} = \{z_i\}$ with $i = 1, \dots, m$. These nodes are used to discretize the normalized fracture within the interval $(-1, 1)$. The Chebyshev polynomials ($\phi(s)$ and $\psi(z)$) have their roots at these same points. It is due to the density dislocation singularity appearing at the tips, that the choice of the Chebyshev polynomials has been made. It is easy to include the singularity known from linear elastic fracture mechanics (LEFM) within these polynomials by the weight functions. Expressing the singularity with the weight function $\omega(s)$ gives

$$d_s w = \omega(s) F(s), \quad \omega(s) = \frac{1}{\sqrt{1-s^2}} \quad (36)$$

where $F(s)$ is an unknown, non-singular function. For such a square-root singularity, as observed in Eq. (36), the corresponding polynomials are the first $\phi_n(s) = T_n(s)$ and second $\psi_m(z) = U_m(z)$ kind of Chebyshev polynomials (with $m = n - 1$). For optimal distribution of nodes, their set is given by (following Viesca and Garagash (2018))

$$s_j = \cos\left(\frac{\pi(j-1/2)}{n}\right), j = 1, \dots, n; \quad z_i = \cos\left(\frac{\pi i}{n}\right), i = 1, \dots, n-1 \quad (37)$$

B.2. Elasticity for an axi-symmetric fracture

The elastic boundary integral Eq. (2) can be inverted to work with the following integral equation relating net pressure and the dislocation density

$$p(x) = \int_0^R G(x, \xi) \frac{\partial w}{\partial \xi} d\xi$$

where the kernel G is obtained from the ring dislocation solution (Hills et al., 1996):

$$G(\xi, \xi') = \begin{cases} \text{sign}(\xi\xi') \left[\frac{1}{\xi-\xi'} \mathbf{E}(k) - \frac{1}{\xi} \mathbf{K}(k) \right], & |\xi'| < |\xi| \\ \frac{1}{\xi-\xi'} \mathbf{E}(1/k), & |\xi'| > |\xi| \end{cases}$$

For an axisymmetric fracture, the kernel is to the leading order of the Cauchy type like for plane-strain fracture, but it also contains a weaker logarithm singularity. Similarly to Liu et al. (2019), we write it as:

$$G(z, s) = \frac{1}{z-s} + \frac{\ln|z-s|}{2z} + \Delta G(z, s) \quad (38)$$

where $\Delta G(z, s)$ corresponds to the non-singular part of $G(z, s)$. In order to maintain the accuracy of the quadrature in this case, we represent the logarithm-term as an integral of the Cauchy-like term, $\ln|z-s| = \int_0^z \frac{dz}{z-s} + \ln s$, where the latter term is inconsequential (it gives zero contribution to the elasticity integral). Using integration on the \mathbf{z} -grid for the logarithm-term, the final elasticity matrix for axisymmetric fracture can be written as:

$$\mathbb{G} = \mathbb{H} + \frac{1}{2z} \mathbb{T} \cdot \mathbb{H} + \Delta \mathbb{G} \quad (39)$$

where $\mathbb{T} = \{T_{ij}\}$ is the \mathbf{z} -grid integration matrix and $\Delta \mathbb{G} = \{\frac{1}{n} \Delta G(z_i, s_j)\}$, and \mathbb{H} is the discretized form of the Hilbert transform

$$H_{ij} = \frac{1}{n} \frac{1}{z_i - s_j} \quad (40)$$

B.3. Discretized form of the set of equations

The dimensionless form of the system of equations for this zero-toughness solution given by Eqs. (15b)–(15d) can be discretized using a collocation method on the \mathbf{z} -points of the chosen Gauss–Chebyshev quadrature. The primary unknowns are the value of F at the n \mathbf{s} -points and the dimensionless fracture length $\gamma_{m0}^{[V]}$.

- Using the discretized Hilbert transformation on Eq. (15b), one obtains after integration from z_i to the tip, the following system of $n-1$ equations

$$\frac{1}{9} \mathbf{z} + \frac{1}{4} (\mathbb{S} \cdot \mathbf{F})^2 \mathbb{D} \cdot \mathbb{G} \cdot \mathbf{F} = 0 \quad (41)$$

where $\mathbf{z} = (z_1, \dots, z_i, \dots, z_{n-1})$ is the vector of the coordinates of the \mathbf{z} -points, and $\mathbf{F} = (F_1, \dots, F_i, \dots, F_n)$ the vector of unknown values of F at the \mathbf{s} -points. \mathbb{D} represents the Barycentric differentiation matrix on the \mathbf{z} -grid and \mathbb{S} the integration matrix from \mathbf{z} to the fracture tip (see Viesca and Garagash (2018) for details).

- The propagation criterion (zero stress intensity factor) reduces to the following scalar equation

$$\mathbf{Q} \cdot \mathbf{F} = 0 \quad (42)$$

where \mathbf{Q} is the Barycentric interpolation vector allowing to obtain the value of F at the fracture tip (and thus the stress intensity factor).

- The global volume balance (15d) becomes after discretization:

$$\mathbb{S}_H \cdot (\mathbf{S}^2 \mathbf{F}) + \frac{1}{\pi \left(\gamma_{m0}^{[V]} \right)^3} = 0 \quad (43)$$

where \mathbb{S}_H is the integration matrix (from 0 to 1).

These $n+1$ discretized non-linear equations allow solving for the n unknown values of F on the \mathbf{s} -grid and the dimensionless fracture length $\gamma_{m0}^{[V]}$.

B.4. Results

We use the built-in Newton scheme of Mathematica (version 12) to solve the non-linear system (41)–(43) using $n = 500$ points. We notably obtain the following value for the dimensionless fracture length: $\gamma_{m0}^{[V]} \approx 0.8360$.

The obtained solution has been verified against the numerical 3D planar HF simulator PyFrac (Zia and Lecampion, 2019) and the 1D HF simulator developed in Lecampion and Desroches

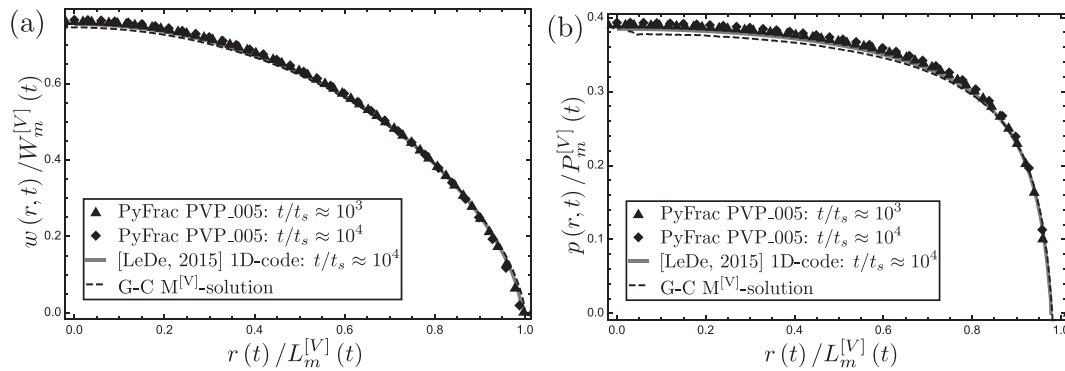


Fig. 10. Dimensionless opening (a) and dimensionless pressure (b). Black dashed lines correspond to the semi-analytical viscosity solution (i.e. $M^{[V]}$ -solution) obtained by the use of Gauss–Chebyshev polynomials ($n = 500$). Black markers show numerical solutions of simulations with PyFrac, and the gray line is the solution of the 1D planar HF Mathematica code described in Lecampion and Desroches (2015).

Table 6

Relative difference between solutions obtained numerically and the results from the self-similar Gauss–Chebyshev collocation scheme. PyFrac simulations (PVP_003 and PVP_005) and a simulation of the code described in Lecampion and Desroches (2015). $\mathcal{E} = \frac{\int_0^1 f_N(\rho) d\rho - \int_0^1 f_{CC}(\rho) d\rho}{\int_0^1 f_{CC}(\rho) d\rho}$ where f_N is an interpolation function of the numerical results and f_{CC} the solution obtained via the Gauss–Chebyshev collocation scheme. The L_2 and L_∞ norms follow their usual definition.

| Simulation | t/t_s | \mathcal{E}_p [%] | $L_{2,p}$ [–] | \mathcal{E}_w [%] | $L_{2,w}$ [–] | $L_\infty(p(0,t))$ [%] | $L_\infty(w(0,t))$ [%] | $L_2(R(t)) = L_\infty(R(t))$ [%] |
|--------------|---------|---------------------|---------------|---------------------|---------------|------------------------|------------------------|----------------------------------|
| PVP_003 | 10^3 | 5.13 | 2.22 | 2.67 | 2.98 | 3.90 | 4.85 | 2.75 |
| | 10^4 | 6.59 | 2.88 | 3.42 | 11.32 | 5.76 | 6.20 | 3.46 |
| PVP_005 | 10^3 | 2.29 | 1.15 | 1.12 | 1.76 | 3.24 | 2.00 | 1.16 |
| | 10^4 | 3.53 | 1.05 | 1.47 | 1.78 | 0.01 | 2.64 | 1.57 |
| [LeDe, 2015] | 10^3 | 1.27 | 1.50 | 0.69 | 2.47 | 1.13 | 1.27 | 0.66 |
| | 10^4 | 1.13 | 1.55 | 0.60 | 2.34 | 1.36 | 1.09 | 0.59 |

(2015). Fig. 10 shows the opening (a) and pressure profiles (b) from the numerical simulations compared to the semi-analytical Gauss–Chebyshev solution obtained in B.4. We evaluate the relative difference of the numerical solutions with the Gauss–Chebyshev collocation scheme for the dimensionless radius, dimensionless inlet opening, and net pressure. All these relative differences are reported in Table 6, for two PyFrac simulations with two different grid (61×61 , respectively 121×121 , elements for PVP_003, respectively PVP_005) and a simulation (using a grid with 80 elements) with the 1D code of Lecampion and Desroches (2015).

The relative difference of the PyFrac simulation reduces with finer mesh. For the coarse mesh used, the relative difference in fracture radius is at most 3.5 percent. We use such a mesh resolution for all the ~ 450 simulations reported in the main text. We use thresholds of 2.5% throughout the paper and then adapt the obtained values to account for the slightly larger uncertainty induced by the numerical error. The 1D numerical results (using a grid with 80 elements) are closer to the one obtained with Gauss–Chebyshev quadrature which is consistent with the fact that the axisymmetric geometry is built-in. The geometrical error on the fracture circular shape is null like for the Gauss–Chebyshev quadrature, contrary to a planar 3D scheme.

References

Abé, H., Keer, L.M., Mura, T., 1976. Growth rate of a penny-shaped crack in hydraulic fracturing of rocks 2. *Journal of Geophysical Research* 81, 6292–6298.
 Anderson, D.G., 1965. Iterative procedures for nonlinear integral equations. *Journal of the ACM (JACM)* 12 (4), 547–560.
 Atkinson, B.K., 1984. Subcritical crack growth in geological materials. *Journal of Geophysical Research: Solid Earth* 89 (B6), 4077–4114.
 Atkinson, B.K., 1987. *Fracture Mechanics of Rock*. Elsevier.
 Barabati, A.C., Desroches, J., Robisson, A., McKinley, G.H., 2016. Complex fluids and hydraulic fracturing. *Annual Review of Chemical and Biomolecular Engineering* 7, 415–453.

Batchelor, G., 1967. *An Introduction to Fluid Dynamics*. Cambridge University Press, Cambridge, UK.
 Boone, T.J., Ingraffea, A.R., 1990. A numerical procedure for simulation of hydraulically-driven fracture propagation in poroelastic media. *International Journal for Numerical and Analytical Methods in Geomechanics* 14 (1), 27–47.
 Bungier, A.P., Detournay, E., 2007. Early-time solution for a radial hydraulic fracture. *Journal of Engineering Mechanics* 133 (5), 534–540.
 Bungier, A.P., Detournay, E., 2008. Experimental validation of the tip asymptotics for a fluid-driven crack. *Journal of the Mechanics and Physics of Solids* 56, 3101–3115.
 Charles, R.J., 1958a. Static fatigue of glass. i. *Journal of Applied Physics* 29 (11), 1549–1553.
 Charles, R.J., 1958b. Static fatigue of glass. ii. *Journal of Applied Physics* 29 (11), 1554–1560.
 De Pater, H., Desroches, J., Groenenboom, J., Weijers, L., 1996. Physical and numerical modeling of hydraulic fracture closure. *SPE Production & Facilities* 11 (02), 122–128.
 Desroches, J., Thiercelin, M., 1993. Modelling the propagation and closure of micro-hydraulic fractures. *International Journal of Rock Mechanics and Mining Sciences & Geomechanics Abstracts* 30 (7), 1231–1234.
 Detournay, E., 2004. Propagation regimes of fluid-driven fractures in impermeable rocks. *International Journal of Geomechanics* 4 (1), 35.
 Detournay, E., 2016. Mechanics of hydraulic fractures. *Annual Review of Fluid Mechanics* 48, 311–339.
 Detournay, E., Cheng, A.H.D., 1991. Plane strain analysis of a stationary hydraulic fracture in a poroelastic medium. *International Journal of Solids and Structures* 27 (13), 1645–1662.
 Detournay, E., Cheng, A.-D., Roegiers, J.-C., McLennan, J., 1989. Poroelasticity considerations in In-Situ stress determination by hydraulic fracturing. *International Journal of Rock Mechanics and Mining Sciences & Geomechanics Abstracts* 26 (6), 507–513.
 Dontsov, E.V., 2016. An approximate solution for a penny-shaped hydraulic fracture that accounts for fracture toughness, fluid viscosity and leak-off. *Royal Society Open Science* 3, (12) 160737.
 Dontsov, E., Peirce, A.P., 2017. A multiscale implicit level set algorithm (ILSA) to model hydraulic fracture propagation incorporating combined viscous, toughness, and leak-off asymptotics. *Computer Methods in Applied Mechanics and Engineering* 313, 53–84.
 Economides, M.J., Nolte, K.G., 2000. *Reservoir Stimulation*. John Wiley & Sons.
 Erdogan, F., Gupta, G.D., Cook, T., 1973. Numerical solution of singular integral equations. In: *Methods of Analysis and Solutions of Crack Problems*. Springer, pp. 368–425.
 Froger, J.L., Fukushima, Y., Briole, P., Staudacher, T., Souriot, T., Villeneuve, N., 2004. The deformation field of the august 2003 eruption at piton de la fournaise.

- reunion island, mapped by asar interferometry. *Geophysical Research Letters* 31 (14).
- Fukushima, Y., Cayol, V., Durand, P., 2005. Finding realistic dike models from interferometric synthetic aperture radar data: The february 2000 eruption at piton de la fournaise. *Journal of Geophysical Research: Solid Earth* 110 (B3).
- Fukushima, Y., Cayol, V., Durand, P., Massonnet, D., 2010. Evolution of magma conduits during the 1998–2000 eruptions of piton de la fournaise volcano, réunion island. *Journal of Geophysical Research: Solid Earth* 115 (B10).
- Garagash, D.I., 2006a. Plane-strain propagation of a fluid-driven fracture during injection and shut-in: asymptotics of large toughness. *Engineering Fracture Mechanics* 73 (4), 456–481.
- Garagash, D.I., 2006b. Propagation of a plane-strain fluid-driven fracture with a fluid lag: early-time solution. *International Journal of Solids and Structures* 43, 5811–5835.
- Garagash, D.I., Detournay, E., Adachi, J.I., 2011. Multiscale tip asymptotics in hydraulic fracture with leak-off. *Journal of Fluid Mechanics* 669, 260–297.
- Germanovich, L.N. and Murdoch, L.C. (2010). Injection of solids to lift coastal areas. In: *Proceedings of the Royal Society of London A: Mathematical, Physical and Engineering Sciences*, volume 466, pages 3225–3252. The Royal Society..
- Gordeliy, E., Detournay, E., 2011. Displacement discontinuity method for modeling axisymmetric cracks in an elastic half-space. *International Journal of Solids and Structures* 48 (19), 2614–2629.
- Gu, H., Leung, K.H., 1993. 3d numerical simulation of hydraulic fracture closure with application to minifracture analysis. *Journal of Petroleum Technology* 45 (03), 206–255.
- Hills, D.A., Kelly, P.A., Dai, D.N., Korsunsky, A.M. (1996). *Solution of crack problems: the distributed dislocation technique*, volume 44 of *Solid Mechanics and its Applications*. Kluwer Academic Publ., Dordrecht..
- Jeffrey, R.G., Chen, Z., Mills, K.W., Pegg, S., 2013. Monitoring and measuring hydraulic fracturing growth during preconditioning of a roof rock over a coal longwall panel. In: *ISRM International Conference for Effective and Sustainable Hydraulic Fracturing*. ISRM, International Society for Rock Mechanics and Rock Engineering, Brisbane, Australia.
- Kanin, Evgenii A., Dontsov, Egor V., Garagash, Dmitry I., Osipov, Andrei A., 2020. A radial hydraulic fracture with pressure-dependent leak-off. *Journal of the Mechanics and Physics of Solids* 143 (104062).
- Lecampion, B., Desroches, J., 2015. Simultaneous initiation and growth of multiple radial hydraulic fractures from a horizontal wellbore. *Journal of the Mechanics and Physics of Solids* 82, 235–258.
- Lecampion, B., Detournay, E., 2007. An implicit algorithm for the propagation of a hydraulic fracture with a fluid lag. *Computer Methods in Applied Mechanics and Engineering* 196, 4863–4880.
- Lecampion, B., 2019. Slickwater hydraulic fracture propagation: near-tip and radial geometry solutions. *Journal of Fluid Mechanics* 880, 514–550.
- Lecampion, B., Desroches, J., Jeffrey, R.G., Bunger, A.P., 2017. Experiments versus theory for the initiation and propagation of radial hydraulic fractures in low permeability materials. *Journal of Geophysical Research: Solid Earth* 122.
- Lecampion, B., Bunger, A.P., Zhang, X., 2018. Numerical methods for hydraulic fracture propagation: A review of recent trends. *Journal of Natural Gas Science and Engineering* 49, 66–83.
- Lister, J.R., Kerr, R.C., 1991. Fluid-mechanical models of crack propagation and their application to magma transport in dykes. *Journal of Geophysical Research: Solid Earth* 96 (B6), 10049–10077.
- Liu, D., Lecampion, B., Garagash, D.I., 2019. Propagation of a fluid-driven fracture with fracture length dependent apparent toughness. *Engineering Fracture Mechanics* 2019, <https://doi.org/10.1016/j.engfracmech.2019.106616>.
- Lu, G., Gordeliy, E., Prioul, R., Bunger, A., 2017. Modeling initiation and propagation of a hydraulic fracture under subcritical conditions. *Computer Methods in Applied Mechanics and Engineering* 318, 61–91.
- Madyarova, M., 2003. *Fluid-driven Penny-shaped Fracture in Permeable Rock* Master's thesis. University of Minnesota, Minneapolis, MN, USA.
- Mohammadnejad, T., Andrade, J.E., 2016. Numerical modeling of hydraulic fracture propagation, closure and reopening using XFEM with application to in-situ stress estimation. *International Journal for Numerical and Analytical Methods in Geomechanics* 40 (15), 2033–2060.
- Moukhtari, F.E., Lecampion, B., Zia, H., 2020. Planar hydraulic fracture growth perpendicular to the isotropy plane in a transversely isotropic material. *Journal of the Mechanics and Physics of Solids* 137, 103878.
- Nolte, K.G., 1979. Determination of fracture parameters from fracturing pressure decline. In: *Proc. SPE Annual Technical Conference and Exhibition*, Las Vegas. SPE 8341.
- Papanastasiou, P., 2000. Hydraulic fracture closure in a pressure-sensitive elastoplastic medium. *International Journal of Fracture* 103 (2), 149–161.
- Pearce, A., 2015. Modeling multi-scale processes in hydraulic fracture propagation using the implicit level set algorithm. *Computer Methods in Applied Mechanics and Engineering* 283, 881–908.
- Pearce, A.P., 2016. Implicit level set algorithms for modelling hydraulic fracture propagation. *Philosophical Transactions of the Royal Society of London A: Mathematical, Physical and Engineering Sciences* 374 (2078), 20150423.
- Pearce, A.P., Detournay, E., 2008. An implicit level set method for modeling hydraulically driven fractures. *Computer Methods in Applied Mechanics and Engineering* 197 (33–40), 2858–2885.
- Rice, J., 1968. A path independent integral and the approximate analysis of strain concentration by notches and cracks. *Journal of Applied Mechanics* 35, 379–386.
- Rice, J.R., 1972. Some remarks on elastic crack-tip stress fields. *International Journal of Solids and Structures* 8, 751–758.
- Rivalta, E., Taisne, B., Bunger, A., Katz, R., 2015. A review of mechanical models of dike propagation: Schools of thought, results and future directions. *Tectonophysics* 638, 1–42.
- Savitski, A., Detournay, E., 2002. Propagation of a penny-shaped fluid-driven fracture in an impermeable rock: asymptotic solutions. *International Journal of Solids and Structures* 39 (26), 6311–6337.
- Settari, A., Cleary, M.P., 1984. Three-dimensional simulation of hydraulic fracturing. *Journal of Petroleum Technology* 36 (07), 1177–1190.
- Smith, M.B., Montgomery, C.T., 2015. *Hydraulic Fracturing*. Crc Press.
- Smittarello, D., Cayol, V., Pinel, V., Peltier, A., Froger, J.-L., Ferrazzini, V., 2019. Magma propagation at piton de la fournaise from joint inversion of insar and gnss. *Journal of Geophysical Research: Solid Earth* 124 (2), 1361–1387.
- Sneddon, I.N., 1946. The distribution of stress in the neighbourhood of a crack in an elastic solid. *Proceedings of the Royal Society. Series A* 187 (1009), 229–260.
- Sneddon, I., 1951. *Fourier Transforms*. McGraw-Hill, New York NY.
- Spence, D., Sharp, P., Turcotte, D., 1987. Buoyancy-driven crack propagation: a mechanism for magma migration. *Journal of Fluid Mechanics* 174, 135–153.
- van Dam, D.B., de Pater, C.J., Romijn, R., 2000. Analysis of hydraulic fracture closure in laboratory experiments. *SPE Production & Facilities* 15 (03), 151–158.
- Viesca, R.C., Garagash, D.I., 2018. Numerical methods for coupled fracture problems. *Journal of the Mechanics and Physics of Solids* 113, 13–34.
- Villeneuve, N., Neuville, D.R., Boivin, P., Bachèlery, P., Richet, P., 2008. Magma crystallization and viscosity: A study of molten basalts from the piton de la fournaise volcano (la réunion island). *Chemical Geology* 256 (3), 242–251.
- Walker, H.F., Ni, P., 2011. Anderson acceleration for fixed-point iterations. *SIAM Journal on Numerical Analysis* 49 (4), 1715–1735.
- Winner, R.A., Lu, G., Prioul, R., Aidagulov, G., Bunger, A.P., 2018. Acoustic emission and kinetic fracture theory for time-dependent breakage of granite. *Engineering Fracture Mechanics* 199, 101–113.
- Zanganeh, B., Clarkson, C.R., Hawkes, R.V., 2017. Reinterpretation of fracture closure dynamics during diagnostic fracture injection tests. p. 18..
- Zia, H., Lecampion, B., 2019. Explicit versus implicit front advancing schemes for the simulation of hydraulic fracture growth. *International Journal for Numerical and Analytical Methods in Geomechanics* 43 (6), 1300–1315.
- Zia, H., Lecampion, B., 2020. Pyfrac: A planar 3d hydraulic fracture simulator. *Computer Physics Communications*, 107368.
- Zia, H., Lecampion, B., Zhang, W., 2018. Impact of the anisotropy of fracture toughness on the propagation of planar 3D hydraulic fracture. *International Journal of Fracture* 211 (1–2), 103–123.